nanomaterials

MDPI

Review

Properties, Preparation and Applications of Low Dimensional Transition Metal Dichalcogenides

Lei Yang [1,*], Chenggen Xie [1], Juncheng Jin [1], Rai Nauman Ali [2], Chao Feng [2], Ping Liu [2] and Bin Xiang [2,*]

[1] Key Laboratory of Biomimetic Sensor and Detecting Technology of Anhui Province, School of Materials and Chemical Engineering, West Anhui University, Lu'an 237012, China; cgxie@wxc.edu.cn (C.X.); jjc@wxc.edu.cn (J.J.)

[2] Department of Materials Science & Engineering, CAS key Lab of Materials for Energy Conversion, Synergetic Innovation Center of Quantum Information & Quantum Physics, University of Science and Technology of China, Hefei 230026, China; nauman@mail.ustc.edu.cn (R.N.A.); fengchao901008@163.com (C.F.); 15209835824@163.com (P.L.)

* Correspondence: leiyang@wxc.edu.cn (L.Y.); binxiang@ustc.edu.cn (B.X.)

Received: 6 June 2018; Accepted: 22 June 2018; Published: 26 June 2018

Abstract: Low-dimensional layered transition metal dichalcogenides (TMDs) have recently emerged as an important fundamental research material because of their unique structural, physical and chemical properties. These novel properties make these TMDs a suitable candidate in numerous potential applications. In this review, we briefly summarize the properties of low-dimensional TMDs, and then focus on the various methods used in their preparation. The use of TMDs in electronic devices, optoelectronic devices, electrocatalysts, biosystems, and hydrogen storage is also explored. The cutting-edge future development probabilities of these materials and numerous research challenges are also outlined in this review.

Keywords: low dimensional transition metal dichalcogenides; crystal structure; electronic structure; preparation methods; chemical vapor deposition

1. Introduction

Since graphene prepared by the mechanical exfoliation method was first discovered in 2004 [1], it sparked a research boom of other kinds of analogous layered structured materials [2–11]. The layered transition metal dichalcogenides (TMDs) is an important kind of layered research material [12–17]. The generalized formula of layered TMDs is MX_2, where X represents a chalcogen e.g., S, Se, Te, and M represents the transition metal atoms in Group 4–7 and in part of Group 8–10 [18], such as Mo, W, Ti, Hf, Re, etc. In each layer of TMDs, the metal atoms are sandwiched by chalcogen atoms with strong chalcogen-metal covalent bond interactions [19]. However, the interlayers stacking is coupled by weak van der Waals forces, which enables the easy exfoliation of bulk crystals into the two-dimensional morphology [18,19]. Similar to graphene, TMDs also display interesting layer-dependent properties, when their thickness decreases from three dimensions to two. For example, bulk MoS_2 is an indirect band gap material with a band gap of 1.3 eV [20]. However, monolayer MoS_2, noticeably different from the bulk, is a direct band gap material with a band gap of 1.9 eV [21]. This indirect-to-direct band gap transition results in the dramatic enhancement of photoluminescence (PL), which can be attributed to quantum confinement and surface effects [19,21,22]. In monolayer TMDs, the lack of inversion symmetry combined with spin-orbit coupling leads to coupled spin and valley physics, which makes it possible to control the spin and valley in these monolayered materials; this doesn't exist in multilayer ones [23,24]. Meanwhile, the experiment has realized the optical pumping of a

single valley (and spin) with circular polarized light [25,26]. As the dimensions of two-dimensional (2D) TMDs are reduced to one-dimensional (1D) and zero-dimensional (0D), the edge effects become much more prominent [27–29]. As predicated by theoretical studies, the electronic structures and properties, together with the quantum confinement effects of these 1D TMDs nanoribbons/nanobelts and 0D TMDs quantum dots (QDs), dramatically changed [27–29].

These novel properties promote the exploration of new methods to prepare the low-dimensional TMDs. Numerous methods are available for their synthesis—mechanical exfoliation [30,31], solution-based exfoliation [29,32–34], Li-intercalation exfoliation [35,36], laser and plasma-induced thinning [37,38], hydrothermal method [39,40] chemical vapor deposition (CVD) [41–50], annealing of the $(NH_4)_2MoS_4$ precursor [51,52], chemical vapor transport [53,54], and so on. Driven by advanced preparation methods and increased research interests, applications based on low-dimensional TMDs have enabled scientists to conquer the appealing properties of these materials. Take MoS_2 as an example—the room temperature on/off ratio of monolayer MoS_2 exceeds 10^8, and in-plane carrier mobility can reach 200–500 $cm^2/V{\cdot}s$ [31]. Furthermore, low-dimensional TMDs have shown excellent electrocatalytic performance in water splitting [55–58].

Several review papers have summarized the structures and properties of two-dimensional TMDs as well as their applications, such as energy storage and conversion, optoelectronic, electrocatalysis, electrochemical biosensors, and so on [59–69]. In this paper, the focus is mainly on the preparation of low-dimensional TMDs, including 2D thin layers, 1D nanoribbons/nanobelts/nanotubes, and 0D QDs. We initially induce the properties of low-dimensional TMDs. The recent progress of various methods to prepare such materials is then explored. Sequentially, their achieved progress for applications in electronic devices, optoelectronic devices, electrocatalysts, hydrogen storage and biosystems is also discussed. In the end, we summarize possible future research directions and potential challenges.

2. Properties and Characterization

2.1. Crystal Structure

Bulk-layered TMDs are composed of X-M-X sandwich layers with interlayer spacing of ~6.5 Å [31,70], as shown in Figure 1a. With different coordination spheres of the transition metal atoms, each individual sandwich layer exhibits several structural phases in which the trigonal prismatic (2H, the prefix '2' is irrelevant in monolayers) or octahedral (1T) is commonly observed, as shown in Figure 1b [59,71]. The Mo atoms in 2H phase are prismatically coordinated to six surrounding S atoms. However, in the 1T phase, six S atoms form a distorted octahedron around one transition metal atom [19,70]. From a side view, the 2H phase is characterized by an AbA stacking order and the 1T phase corresponds to an AbC stacking order, where the capital and lower letters correspond to metal and chalcogen atomic planes, respectively. With different polymorphs and stacking sequence, the bulk TMDs present three polytypes: 1T, 2H and 3R, where the digits correspond to the number of layers in the stacking sequence, and the letters stand for trigonal, hexagonal and rhombohedral, respectively [18]. The schematic structures are shown in Figure 1c [70]. In bulk TMDs formed by group VI transition metals (metal = Mo or W; chalcogen = S, Se or Te, except WTe_2), 2H is a thermodynamically stable phase and 1T is a metastable phase [59]. For example, in MoS_2, the molybdenite is commonly found in 2H phase [18]. The 1T-MoS_2 is a metastable metallic phase, which will undergo a first order phase transition and transform into the thermodynamically stable form of 2H-MoS_2 when the temperature is higher than 100 °C [72]. Suenaga's group systematically studied the structural transformation between the semiconducting (2H) and metallic (1T) phases in atomic resolution by using in situ scanning transmission electron microscopy (TEM) technique [73]. Their results indicated that the 2H/1T phase transition involved intra layer sulphur and/or molybdenum atomic plane gliding and required an intermediate phase (α-phase) as a precursor (Figure 1d) [73]. Moreover, the 1T-MoS_2 is often prepared by the Li intercalation method [36,72,74]. Recently, Zhang's group also synthesized 1T'-MoX_2 (X = S, Se) crystals with lateral size up to hundreds of micrometers. The 1T' is a lower-symmetry phase,

which is a distorted version of the 1T structure as shown in Figure 1b [71,75]. The 1T′-MoX_2 (X = S, Se) is a metastable phase, which is convertible to the 2H-MoS_2 phase after thermal annealing or laser irradiation. Similar to the 2H phase, the 3R phase shows semiconducting behavior and often exists in the synthetic MoS_2 [18,76]. In contrast to traditional 2H-Mo(W)S_2 and Mo(W)Se_2, the group IV and V TMDs compounds such as TiS_2 and $TaSe_2$ are observed in 1T phase under ambient conditions [71,77]. However, for the WTe_2, the 1T′ phase is more stable than its hexagonal-phase structure, according to theoretical calculations and experimental results [78,79].

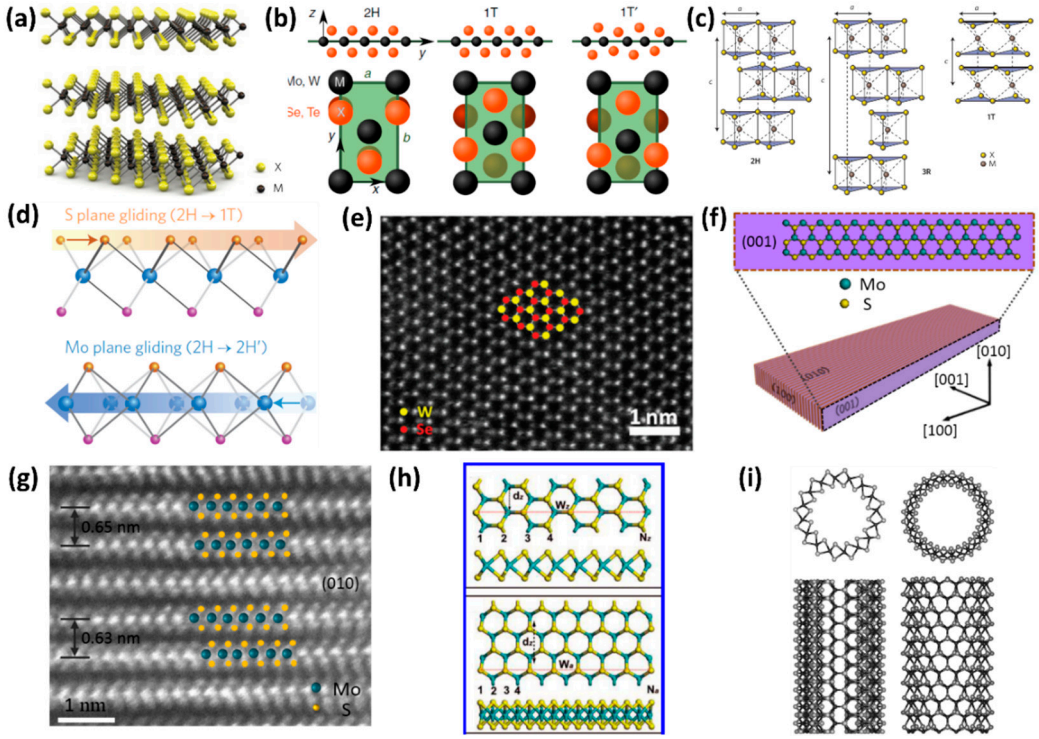

Figure 1. Structure of low-dimensional TMDs. (**a**) Three-dimensional schematic representation of a typical MX_2 structure. The yellow balls and grey balls refer to chalcogen atoms and transition metal atoms, respectively [70]. (**b**) The layer structure (**top**) and rectangular unit cell (**down**) of 2H, 1T and 1T′ phases. The 2H phase refer to trigonal prismatic structure, 1T and 1T′are called octahedral and distorted octahedral, respectively [71]. (**c**) Schematic structure of 2H, 3R and 1T phase of MX_2. The interlayer spacing is ~6.5 Å and the stacking index c indicates the number of layers in each stacking order [70]. (**d**) Schematic illustration of the gliding of S plane (**top**) and Mo plane (**bottom**), which result in phase transition. The S plane glide results in a 2H → 1T phase transition, and Mo plane glide results in a 2H → 2H′ transition, where the 2H′ phase is a 60° rotational phase of 2H [73]. (**e**) HRSTEM image of monolayer WSe_2 with defect-free atomic lattices. The W and Se atoms form the hexagonal ring with different brightness as denoted by the color cartoon spheres [43]. (**f**,**g**) Schematic illustration and HRSTEM image of MoS_2 nanobelts. The vertical atomic layers form the nanobelt structure, and these layer edges form the top surface of the nanobelt [80]. (**h**) Side and top views of the structures of 8-zigzag MoS_2 nanoribbon (**top**) and 15-armchair MoS_2 nanoribbon (**down**). The W_z (W_a) and d_z (d_a) correspond to the ribbon width and 1-D unit cell distance, respectively [27]. (**i**) Armchair (8, 8) MoS_2 nanotube (**left**) and zigzag (14, 0) MoS_2 nanotube (**right**). The dark and light atoms are Mo and S, respectively [81]. Reproduced with permission from [27]. Copyright American Chemical Society, 2008. Reproduced with permission from [43]. Copyright The Royal Society of Chemistry, 2015. Reproduced with permission from [70]. Copyright Macmillan Publishers Limited, 2012. Reproduced with permission from [71,73]. Copyright Macmillan Publishers Limited, 2014. Reproduced with permission from [80]. Copyright American Chemical Society, 2015. Reproduced with permission from [81]. Copyright The American Physical Society, 2000.

For the edge structure of group VI TMDs compounds, such as MoS_2, it is better to expose two types of low index edge terminations: the $(10\bar{1}0)$ Mo edge and the $(\bar{1}010)$ S edge [82–84]. In the internal of MoS_2 "sandwich" layers, the atoms are all saturated [82,85]. Theoretical calculations indicate that the Mo edges became unstable when the Mo bonds on the edge are unsaturated [82,85]. The edge can be the structure with one S (50% coverage) or two S atoms (100% coverage) per Mo edge atom (called S dimers) due to the fact that the edges have no perfect trigonal prismatic coordination [82,85]. In this condition, the Mo atoms bonding with six S atoms are saturated.

High-resolution scanning TEM (HRSTEM) is an efficient characterization approach to investigate the crystal structure of low-dimensional layered TMDs at the atomic level. Especially in single layer TMDs, it is easy to distinguish M sites and X-X sites [46,72,86,87]. In HRSTEM imaging, the brightness of the atom is proportional to the mean square of the atom's number along the direction of the electron beam [88]. For example, in monolayer WSe_2, the W and Se atoms form a hexagonal ring with different brightness as denoted by the color cartoon spheres in Figure 1e [43]. The brighter dots correspond to the W sites, while the darker dots refer to the Se-Se sites (the atomic number of W and Se atom is 74 and 34, respectively). The atomic number of S is 16, which is smaller than that of Se. If one or two S atoms replace Se-Se sites, the brightness will become darker than that of original Se-Se sites. Therefore, HRSTEM can also be employed to portray the distribution of the chalcogen atoms in the monolayer MX_2 alloy system.

When the dimensions of 2D TMDs materials are reduced, one-dimensional TMDs, such as nanoribbons, nanobelts or nanotubes, are obtained. Recently, our group synthesized single-crystal atomic-layered MoS_2 nanobelts for the first time [80]. HRSTEM characterization indicated that the (001) basal planes of the MoS_2 nanobelts were vertical on the substrate (Figure 1f,g) and the edges of the base planes formed the top surfaces of the nanobelts. Xu et al. also achieved a similar structure, but the MoS_2 nanobelts showed a polycrystalline structure [49]. For TMDs nanoribbons, they usually present "belt" morphologies with the c-axis of base planes vertically aligned to the substrate [27,89–92]. The edges of TMDs nanoribbons were predominant due to its large surface-to-volume ratio. In general, the TMDs nanoribbons usually show zigzag- or armchair-terminated edges, which make the TMDs show different structure-related properties. Figure 1h shows the top and side views of the structure of 8-zigzag-MoS_2 nanoribbon (top) and (b) 15-armchair-MoS_2 nanoribbon (bottom) [27]. The W_z (W_a) and d_z (d_a) correspond to the ribbon width and 1-D unit cell distance, respectively.

Similar to carbon nanotubes, tubular structures can be analogously constructed by twining a 2D triple layer of TMDs around the surface of a cylinder, thus rolling up the sheets along specific directions in the 2D lattice [81,93]. By describing the nanotubes in terms of the primitive 2D lattice vectors and two integer indices $\vec{B} = n\vec{a} + m\vec{b}$, the nanotube could be divided into three classes: $n = m$ "armchair" nanotubes, $n \neq 0$, $m = 0$ "zigzag" nanotubes, and $n \neq m$ "chiral nanotubes" [81]. Figure 1i schematically illustrates the armchair (8, 8) MoS_2 nanotube and zigzag (14, 0) MoS_2 nanotube; a triple layer of atoms created a wall that exhibits certain "roughness" on the outer shell [81].

Further limiting the dimension of the 1D materials, TMDs with small planar dimensions, namely QDs, are obtained. The size of TMDs QDs could be as small as ~2 nm, which contain fewer than 50 molecules, and the thickness could be as small as a triple layer of atoms [94]. Compared to nanosheets, QDs have higher special surface area. Unlike other QDs with dangling bonds on the surface, TMDs QDs have no dangling bonds on their basal planes, except at possible defect sites and edges [29].

2.2. Band Structure and Optical Properties

The various chemical compositions and structural phases make the TMDs a promising candidate for a broad range of electronic properties. Here, we discuss the semi-conductive TMDs formed by group VI transition metals Mo and W, combined with S and Se. In the bulk form of layered TMDs, the conduction band minimum is located at halfway between Γ and K points in Brillouin zone. However, the valence band maximum is located at Γ point, and the valence band sub-maximum and the conduction band sub-minimum coincide at K point [12,21]. By decreasing thickness, the direct excitonic

transition energy at K point does not change, while the indirect band gap increases monotonically [95]. The direct excitonic transition energy becomes larger than the indirect one, when the thickness of TMDs is decreased to the 2D limit, which makes the monolayer TMDs transform into the direct band gap semiconductor (Figure 2a) [95]. It has been established that the energy states of the conduction band at K point mainly originated from the strongly localized d orbitals of Mo atoms, which had minimal interlayer coupling [95]. The states near the Γ point and the point of indirect band gap, however, came from the combination of d orbitals on Mo atoms and antibonding p_z orbitals on S atoms. This is the reason why the band gap energies are sensitive to layer thickness.

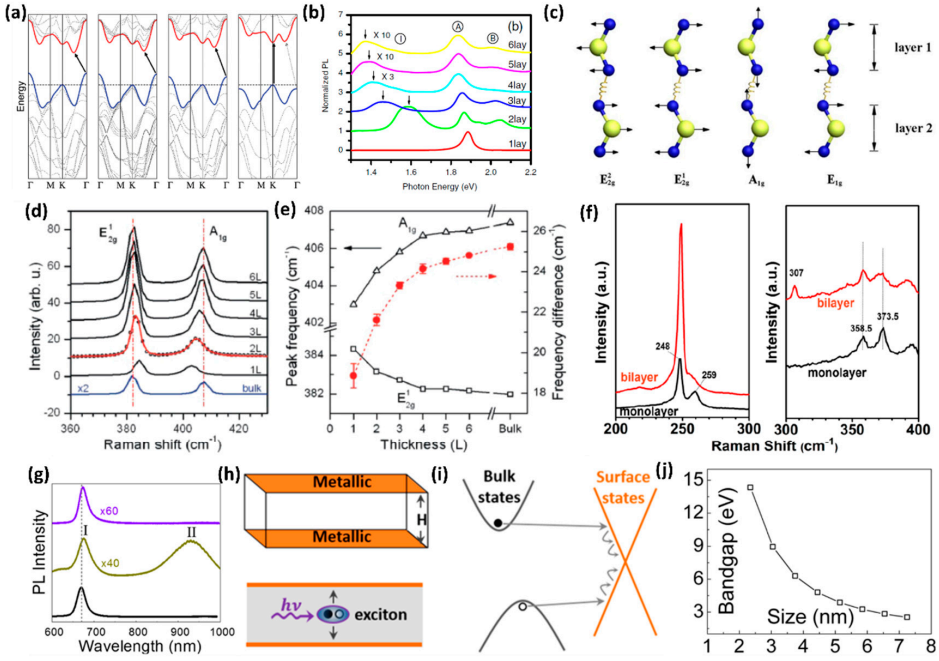

Figure 2. Band structure and optical properties of low-dimensional TMDs. (**a**) Calculated band structures of bulk MoS_2, quadrilayer MoS_2, bilayer MoS_2 and monolayer MoS_2. Bulk MoS_2, quadrilayer MoS_2, bilayer MoS_2 are all indirect band gap materials. When the thickness is reduced, the indirect band gap becomes larger. It becomes direct band gap when the thickness reaches the 2D limit [95]. (**b**) PL spectra of MoS_2 with different thickness (1–6 layers). Peak I corresponds to the indirect band gap transition, while peaks A and B refer to the direct band gap transition [21]. (**c**) Schematic view of the atomic displacements of the four Raman-active modes [39]. (**d**) Raman spectra of MoS_2 with different thickness. With increasing the layer from 1 to 6, the E^1_{2g} shows red shifts, and A_{1g} shows blue shifts [96]. (**e**) The layer dependent of the E^1_{2g} and A_{1g} Raman modes (**left vertical axis**) and the difference of E^1_{2g} and A_{1g} (**right vertical axis**) as a function of layer thickness [96]. (**f**) Raman spectra of monolayer and bilayer WSe_2. For bilayer WSe_2, there was an obvious peak at 307 cm^{-1} which was absent in monolayer one [97]. (**g**) PL spectra of the nanobelt, an exfoliated multilayer, and a CVD-grown monolayer. Compared with exfoliated multilayer, the indirect band gap transition peak nearly disappeared [80]. (**h**,**i**) Scheme of the structure and electronic band picture for the nanobelt. The induced excitons first diffuse to the metallic surface and then nonradiatively decay [80]. (**j**) The relationship between the MoS_2 QDs size and bandgap. With reducing the QDs size, reduced band gap was obtained [29]. Reproduced with permission from [21]. Copyright The American Physical Society, 2010. Reproduced with permission from [29]. Copyright AIP Publishing LLC, 2015. Reproduced with permission from [39]. Copyright Macmillan Publishers Limited, 2014. Reproduced with permission from [80]. Copyright American Chemical Society, 2015. Reproduced with permission from [95,96]. Copyright American Chemical Society, 2010. Reproduced with permission from [97]. Copyright American Chemical Society, 2013.

PL measurement is an effective characterization method that reflects the evolution of electronic structure of TMDs with various thicknesses. For instance, the PL spectra intensity of bulk MoS_2 can be neglected. When the thickness is decreased to a few layers, like 2–6 layers, the MoS_2 samples display multiple emission peaks, as shown in Figure 2b [21]. Peaks labeled A and B correspond to the direct excitonic transitions at the Brillouin zone K point, while the Peak I corresponds to the indirect band gap transition [21]. It is obvious that the PL intensity becomes much stronger when the thickness is reduced to the monolayer; this is mainly due to the fact that the band gap is transformed from indirect one to the direct one [19,21,22]. Surprisingly, when the lateral dimensions of metallic 2D TMDs are reduced, similar PL responses are observed [98,99]. This might be due to the spatial quantum confinement effect of the electron clouds, similar to observations in other metallic nanoparticles [98]. Besides the PL spectra, the Raman spectra are also relevant to the thickness of layered TMDs and can be used to characterize their electronic properties [96,97,100]. Figure 2c shows the atomic displacements of the four Raman-active modes of MoS_2 or WSe_2 [39]. In MoS_2, the E_{1g} and $E^2{}_{2g}$ are hardly observed due to selection rules and limited rejection of the Rayleigh scattering [22,26,96]. For the out of-plane A_{1g} mode, the restoring force is mainly from the interlayer van der Waals interaction [101]. With the increase of the number of layers, the restoring forces are enhanced, so that the A_{1g} mode frequency is increased. The in-plane E^1_{2g} mode is a symmetric mode. When the number of layers are increased, the frequency shifts to the lower region. The decrease in frequency is possibly due to the long range Columbic interactions from the coupled dipoles induced from Mo-S bonds [101,102]. Figure 2d shows the representative Raman spectra for monolayer, few-layer (2–6 layers) and bulk MoS_2 samples. With increasing sample thickness, the blue shifts of A_{1g} and red shifts of E^1_{2g} are observed. When the thickness is increased to six layers, the frequencies of E^1_{2g} and A_{1g} modes converge to bulk values [96]. By measuring the frequency difference of E^1_{2g} and A_{1g} active modes, we can verify the thickness of few layers MoS_2 sample. Figure 2e shows the frequencies of E^1_{2g} and A_{1g} Raman modes (left vertical axis) and their difference (right vertical axis) with layer thickness [96]. The frequencies and their difference are also summarized in Table 1. Compared with MoS_2, some second order and combinational modes, like the peak around 307 cm^{-1}, are also observed in the WSe_2 bulk crystal, as shown in Figure 2f [97]. Instead of the E^1_{2g} and A_{1g} active modes, this second order mode peak can be used to confirm its monolayer configuration, because it is absent in monolayer configuration [97,103,104].

Table 1. Frequencies of E^1_{2g} and A_{1g} Raman modes and their difference with different layer thickness.

Thickness (L)	E^1_{2g} (cm^{-1})	A_{1g} (cm^{-1})	Frequency Difference(cm^{-1})
1	~384.4	~403.0	~18.6
2	~383.3	~404.8	~21.5
3	~382.7	~405.8	~23.1
4	~382.3	~406.7	~24.4
5	~382.3	~406.9	~24.6
6	~382.2	~407.0	~24.8
Bulk	~382.0	~407.4	~25.4

For 1D TMDs nanoribbons, the edges are predominant. First-principles computations indicate that the zigzag MoS_2 nanoribbons show metallic behavior, irrespective of ribbon width and thickness [27]. Whereas, the armchair MoS_2 nanoribbons are semiconducting and the band gap is converted to a constant value of 0.56 eV with increasing ribbon width [27]. Furthermore, the zigzag MoS_2 nanoribbons are more stable than the armchair one [27]. This stable metallic edges were verified in the MoS_2 nanobelts experimentally, as mentioned in Section 2.1 [80]. In MoS_2 nanobelts, the PL intensity of direct band gap transition peak was as weak as that in the exfoliated multilayer, which indicated that the nanobelt structure was still an indirect band gap material. However, the indirect band gap transition peak disappeared, as shown in Figure 2g [80]. The disappearing of the indirect band gap transition peak was caused by full metallic edge states, which provided an effective channel for exciton decay.

The top surface was fully composed of metallic edge states, as shown in Figure 2h [80]. Therefore, the excitons (electron-hole pairs) could decay non-radiatively from the edge states (Figure 2i), and the indirect band gap PL peak nearly disappeared. As for nanotubes such as MoS_2, the armchair (n, n) nanotubes exhibit a nonzero moderate direct gap and the zigzag (n, 0) nanotubes possess a narrow direct band gap [81]. Furthermore, the (n, n) tubes show a small indirect gap similar to the direct gap of (n, 0) nanotubes [81].

Different from the 2D and 1D TMDs, the band gap of TMDs QDs have shown size-dependent properties due to quantum confinement. For MoS_2 QDs, The PL peak position indicated a blue-shift as compared to big MoS_2 sheets [29,105]. The smaller the size is, the larger the energy gap will be [29,105]. The band gap of MoS_2 QDs versus particle size is shown in Figure 2j [29]. According to the effective-mass approximation, the correlation between the band gap and size can be derived by the following equation:

$$E = E_g + \frac{h^2}{8\mu r^2} - \frac{1.8e^2}{4\varepsilon_0 \varepsilon r}$$

where μ is the reduced mass of exciton with value of 0.16 m_0 (m_0 is the free-electron mass), h is the Plank's constant, E_g is the indirect band gap value of 1.29 eV, and the dielectric constant is about 6.8.

2.3. Band Gap Engineering

Engineering the electronic structure of layered TMDs is an efficient way to tailor their physical and chemical properties, and is also of great importance to broaden their applications. In the beginning, alloying was an effective approach to tune electronic structures. Xie's group initially realized the tunable band gap in $Mo_{1-x}W_xS_2$ monolayers [106]. By varying the W content in the alloys, the band gap was continuously tuned from 1.82 eV to 1.99 eV, confirmed by the PL spectra [106]. Their results indicated that the band gap energy of monolayer $Mo_{1-x}W_xS_2$ was smaller than the linear combination of that of MoS_2 and WS_2. That is to say, it agreed with the bowing effect as observed in many bulk semiconductor alloys: $E(PL,Mo_{1-x}W_xS_2) < (1-x)E(PL,MoS_2) + xE(PL,WS_2)$ [106]. Our group successfully synthesized the monolayer $MoS_{2(1-x)}Se_{2x}$ and $WS_{2(1-x)}Se_{2x}$ alloys by using the CVD method, and realized the 0.31 eV and 0.4 eV band gap tuning, respectively [107–109].

Exerting strain is another useful way to engineer electronic structures [84–86]. As TMDs can resist large strains before they break, lattice strain engineering is an important strategy to tune their band gap [110–112]. Conley et al. applied uniaxial tensile mechanical strain on monolayer and bilayer MoS_2 to investigate the evolution of their band structure and phonon spectra by using a four-point bending apparatus [112]. The schematic diagram is shown in Figure 3a [111]. By controlling the bend of the substrate, different uniaxial strains were applied to MoS_2 [111]. Measured by PL spectroscopy, they found that the decrease in optical band gap was approximately linear with the strain [111]. The band gap tuning was ~45 meV per 1% strain for monolayer MoS_2 and ~120 meV per 1% strain for bilayer MoS_2. At the same time, they also found that the strain caused the phonon vibration modes to shift to lower frequencies and the degenerate E′ peak to split into two sub-peaks, as shown in Figure 3b. This was mainly due to the fact that the strain broke the symmetry of the crystal [111].

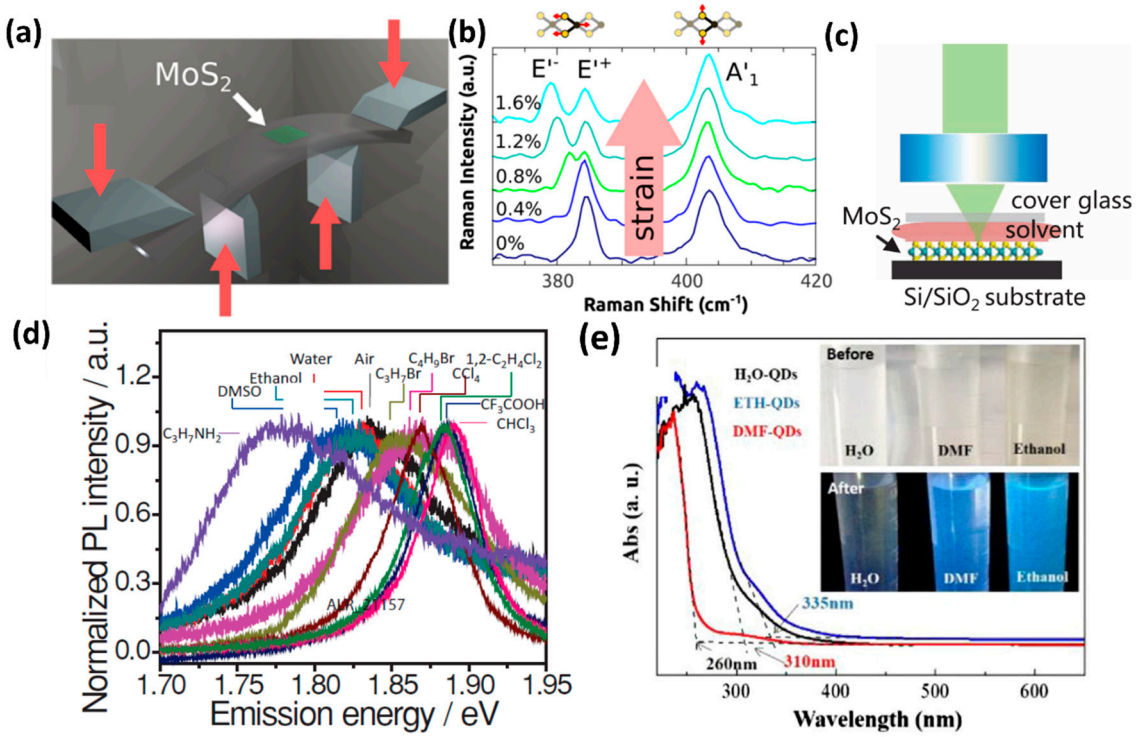

Figure 3. Band gap engineering of low-dimensional TMDs. (**a**) Schematic illustration of the bending apparatus used to exert strain on MoS_2. By controllably bending the polycarbonate beam of the four-point bending apparatus, a uniaxial strain was exerted on monolayer and bilayer MoS_2 [110]. (**b**) Evolution of the Raman spectra with strain ranged from 0 to 1.6%. With increased strain, the symmetry of the crystal broke, which made the degenerate E′ peak split into two sub-peaks [110]. (**c**) Schematic depiction of the micro-Raman-PL experimental configuration. The surface of the monolayer MoS_2 is covered by different solvents during experiments [113]. (**d**) PL spectra of monolayer MoS_2 with different solvent surroundings. The emission peaks were tuned in the range of 1.78–1.90 eV. Red shifts of the monolayer MoS_2 PL peaks were observed when the surroundings changed from air to non-halogenated solvents (water, ethanol, dimethyl sulfoxide, propylamine). Blue shifts were observed when the surroundings changed from air to halogenated solvents (trifluoroacetic acid, methylene chloride, chloroform, carbon tetrachloride, butyl bromide, propyl bromide) [113]. (**e**) UV-visible absorption of functionalized MoS_2 QDs. The absorption edges of MoS_2 QDs in DI water (H_2O-QDs), in DMF and in ethanol were located at ~310 nm, ~260 nm, and ~335 nm, respectively [40]. Reproduced with permission from [40]. Copyright Elsevier Inc., 2017. Reproduced with permission from [110]. Copyright American Chemical Society, 2013. Reproduced with permission from [113]. Copyright Wiley-VCH Verlag GmbH & Co. KGaA, 2013.

Recently, experimental results have also demonstrated that the controlled strain of 2D semiconductors is achieved during CVD growth by utilizing the thermal coefficient of expansion (TCE) mismatch between the substrate and the semiconductor [114]. For example, the TCE of WSe_2 was 9.5 $\pm$ 3.2 ppm, which was much larger than that of aluminum nitride and fused silica with the value of 0.55 and 5.5 ppm, respectively. Therefore, aluminum nitride and fused silica could induce tensile strain on the as-grown WSe_2. The strontium titanate had a TCE of 12 ppm, which yielded compressively strained samples and sapphire had a TCE value closely matched to WSe_2, which could produce relaxed samples. After the growth at high temperature, substrates with stable built-in strains ranging from 1% tensile to 0.2% compressive were achieved. PL characterizations indicated that there was strain-induced indirect-to-direct optical transition in the directly-grown WSe_2 bilayer and brightening of the dark exciton in monolayer WSe_2 [114].

The strain effect could also influence the band gap of TMDs nanotubes and nanoribbons. For example, when the axial tensile strain was exerted on MoS_2 nanotubes, the band gap would decrease for both armchair and zigzag nanotubes [93]. On increasing the axial tensile strain, progressive decrease in band gap was observed. For the armchair nanotubes, however, a semiconductor-to-metal transition happened when the axial tensile strain reached about 8% [93]. Meanwhile, an applied strain could also reduce the band gap of MoS_2 nanoribbons [115].

Besides the strain and alloying, surrounding solvents can also influence the PL spectra of layered TMDs. Xie's group investigated the effect of surrounding solvents on the PL of monolayer MoS_2 [113]. Figure 3c shows a schematic experimental configuration in which the top surface of the MoS_2 monolayer is covered by different solvents during experiments [113]. With different solvent surroundings, the PL spectra of MoS_2 monolayers showed emission peak in the range of 1.78 to 1.90 eV, as shown in Figure 3d [113]. Their results suggested that the PL spectra of monolayer MoS_2 showed blue shifts (up to 60 meV) with halogenated solvent surroundings (trifluoroacetic acid, methylene chloride, chloroform, carbon tetrachloride, butyl bromide, propyl bromide) and red shifts (up to −60 meV) with non-halogenated solvent surroundings (water, ethanol, dimethyl sulfoxide, propylamine), comparing to the PL spectra in air (Figure 3d) [113]. For the red shifts with non-halogenated solvents, it meant more stabilization for the excited state in polar solvents. However, for the halogenated solvents, the special bond between the halogen atoms and the MoS_2 dissociated the negative trions to neutral excitons, which caused an abnormal blue shift of PL spectra [113].

For the MoS_2 nanoribbons, edge passivation was also an effective way to engineer its band structure, because it could fluctuate the edge charge distribution. For example, in armchair MoS_2 nanoribbons, the indirect band gap would be transferred to direct band gap when the edges were passivated by full hydrogen, amidogen or partial hydroxyl [90]. Compared with the bare armchair MoS_2 nanoribbons or the hydrogen passivated MoS_2 nanoribbons, the hydrogen and oxygen hybrid edge-terminated structure was more stable [89]. Different from the band gap of bare armchair MoS_2 nanoribbons (~0.61 eV), the band gap of nanoribbons with hydrogen passivation and with hydrogen and oxygen hybrid passivation were about 0.60 eV and 1.43 eV, respectively [88]. When the armchair MoS_2 nanoribbons were passivated by hydrogen and fluorine (nitrogen, phosphorus) hybrid, the nanoribbons showed metallic behavior [89].

Furthermore, surface passivation was also valid for band gap tuning of TMDs QDs. Our group realized a band gap tunability in MoS_2 QDs passivated by different functional groups [40]. As shown in Figure 3e, the UV-visible absorption spectra characterization indicated that the absorption edge of MoS_2 QDs in DI water was located at ~310 nm, while the absorption edge of MoS_2 QDs dispersed in DMF and ethanol were located at ~260 nm and ~335 nm, respectively. Compared with MoS_2 QDs in ethanol, there was a blue shift of 75 nm (1 eV) observed in the band gap of QDs in DMF. In general, electron-donating and electron-accepting behaviors occurred between the host material and functional groups. When dispersed in ethanol, MoS_2 QDs were mainly functionalized by the hydroxyl groups, which could increase the capacity of the conjugate system by giving π electrons to the host material. The acceptance of the electrons raised the energy level of the highest-occupied molecular orbital of the host material MoS_2 QDs, leading to a decreased band gap. When dispersed in DMF, MoS_2 QDs were mainly functionalized by the aldehyde groups, which could reduce the energy level location of the highest occupied molecular orbital of the host material by withdrawing the electrons from the host material. As a result, an increased band gap was achieved. On varying the concentration of ethanol in distilled water, the band gap of MoS_2 QDs showed a concentration-dependent phenomena: a red shift of ~100 meV on increasing the concentration of ethanol from 10% to 100%. This was caused by the fact that the number of hydroxyl groups in the functionalized ethanol-MoS_2 QDs was different, as varied from the concentration.

An electric field could also be used to modulate the band gap of armchair MoS_2 nanoribbons [116]. Theoretical calculations indicated that the band gap of monolayer armchair MoS_2 nanoribbons could be significantly reduced and closed by a transverse field [116]. However, when the perpendicular field

was applied, the band gap modulation was absent. On increasing the ribbon width, the critical strength of the transverse field for gap closure decreased. In contrast, in multilayer armchair MoS_2 nanoribbons, the band gap can be effectively reduced by both transverse and perpendicular fields [116].

2.4. Mechanical Properties

For the application of bendable electronics in the future, the mechanical properties of layered TMDs should also be characterized. Kis's group investigated the stretching and breaking of monolayer and bilayer MoS_2 by using the nanoindentation in an atomic force microscope (AFM) [117]. During the measurement, the AFM tip was placed above the suspended MoS_2 sample, which was transferred to the pre-patterned SiO_2 substrate containing an array of 550 nm circular holes. The schematic illustration is shown in Figure 4a [117]. They found that the in-plane stiffness of monolayer MoS_2 was 180 ± 60 N/m, corresponding to an effective Young's modulus of 270 ± 100 GPa. This value of Young's modulus was comparable to that of steel. They also observed that the break of MoS_2 appeared at the average strength of 23 GPa, about 11% of its Young's modulus, which meant that the sample was highly crystalline, almost defect-free, and could be used in many high-demand mechanical-related applications [117].

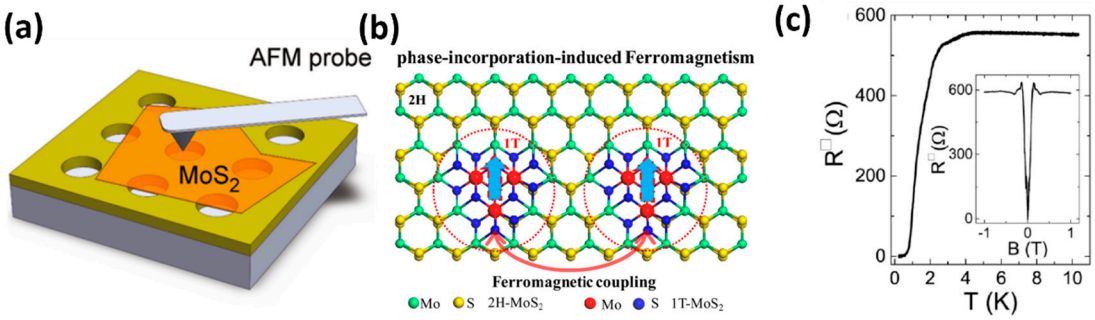

Figure 4. Mechanical, ferromagnetic and superconductivity properties of 2D TMDs. (**a**) Schematic illustration for the stiffness measurements of monolayer MoS_2. During measurements, the AFM tip was placed above the center of the suspend area and slowly lowered while monitoring the deflection [117]. (**b**) Diagrammatic representation of the phase incorporation strategy to achieve ferromagnetism of 2H-MoS_2 nanosheets. By incorporating the 1T-MoS_2 phase into the 2H-MoS_2 matrix, ferromagnetism was induced [118]. (**c**) Temperature dependence of the square resistance of ionic-gated WS_2 FET at V_G = 3.7 V. The resistance decrease was observed with an onset at ~4 K, and the resistance reached zero at Tc ~0.5 K. The inset shows the magnetic field dependence of the square resistance at T = 0.25 K, which indicated that the WS_2 reached the normal state value with magnetic field B ~0.14 T [119]. Reproduced with permission from [117]. Copyright American Chemical Society, 2011. Reproduced with permission from [118,119]. Copyright American Chemical Society, 2015.

Similarly, Kaplan-Ashiri et al. also investigated the mechanical behavior of individual WS_2 nanotubes by attaching the WS_2 nanotube to a commercial silicon AFM cantilever [120]. The cantilever was placed in an AFM and the WS_2 nanotube tip was pushed against the sputtered titanium surface, thus applying a controlled and measurable force. By using the Euler buckling formula, the average Young's modulus of an individual WS_2 nanotube was found to be 171 GPa, which was comparable to that of the bulk material (150 GPa). They also performed First-principle calculations to study the Young's modulus of MoS_2 nanotubes. The calculated results indicated that the armchair (n, n) nanotubes had a considerably smaller Young's modulus than the zigzag (n, 0) nanotubes with a similar radius. By increasing the radius, the Young's modulus of armchair nanotubes increased; however, the Young's modulus of zigzag nanotubes remained essentially invariant with the tube's radius and was very close to that of bulk MoS_2 (238 GPa). Ataca et al. also calculated the mechanical properties of MoS_2 nanoribbons [121]. For armchair MoS_2 nanoribbons (n = 12) and zigzag MoS_2 nanoribbons

(n = 6), the calculated in-plane stiffness was 108.47 and 103.71 N/m, respectively. The difference between the stiffness values of armchair and zigzag nanoribbon was due to the different bonds and edge directions.

2.5. Ferromagnetic Properties

The spin-splitting property make the layered TMDs suitable for spintronics applications [70,122]. However, their applications in spintronics were hampered by their nonmagnetic property. If the room temperature ferromagnetism was endowed to nonmagnetic TMDs materials, the TMDs could be expected to act as an ideal spintronics channel material for nanodevices. Therefore, developing approaches to effectively induce magnetism in TMDs is highly desired. It is remarkable to achieve magnetism in nonmagnetic MoS_2 without magnetic atom doping. In 2007, Zhang et al. synthesized edge-oriented MoS_2 nanosheet-like films by thermal evaporation of the single-source precursor tetrakis (diethylaminodithiocarbomate) molybdate(IV) [123]. Magnetic characterization indicated that MoS_2 nanofilms exhibited weak magnetism (~1–2 emu/g) with a Curie temperature of 685 K. Similar phenomena was also observed in MoS_2 nanobelts [49]. Density functional theory (DFT) calculations demonstrated that magnetism mainly arose from unsaturated atoms at the edge sites. To get a better understanding of magnetism at the edge sites, Li et al. carried out first-principles computations to predict the magnetic properties of MoS_2 nanoribbons with either zigzag- or armchair-terminated edges [27]. For zigzag nanoribbons, they showed that the ferromagnetic and magnetic moment mainly resulted from unsaturated edge atoms. In contrast, armchair nanoribbons were nonmagnetic. The ratio of edge atoms vs. total atoms was very important for magnetic behavior in MoS_2 nanoribbons with zigzag- terminated edges. The magnetism of MoS_2 zigzag nanoribbons became weaker as the ribbon width increased and disappeared in the infinitely single-layered MoS_2 and bulk. This is the reason why nonmagnetic property is observed in common MoS_2.

Besides the zigzag-terminated edges, doping defects on the base plane was also an effective way to induce and manipulate the magnetism of MoS_2 nanosheets [124]. Recently, Wei's Group realized ferromagnetism in MoS_2 at room temperature by using a phase incorporation strategy [118]. During the synthesis, they intentionally introduced sulfur vacancies in 2H-MoS_2 nanosheet by a two-step hydrothermal method. Figure 4b shows the schematic representation of the phase incorporation strategy to achieve ferromagnetism of 2H-MoS_2 nanosheets. The sulfur vacancies could facilitate the transformation of the surrounding 2H-MoS_2 into a 1T-MoS_2 which greatly enhanced the saturation magnetization of 2H-MoS_2 nanosheets at 300 K from 0.02 to 0.25 μB/Mo. Experimental characterizations and calculation results indicated that the ferromagnetism of this incorporated structure originated from exchange interactions between sulfur vacancies and Mo^{4+} ions [118].

2.6. Superconductivity

Superconductivity is another interesting property that exists in TMDs. Group V TMDs compounds like $NbSe_2$ and TaS_2 exhibit intrinsic superconductivity, which has been well elucidated in Ref. [59]. For semiconducting layered TMDs represented by 2H-MoS_2, WS_2 or $MoSe_2$, the realization of low-resistance metallic behavior was the prerequisite to achieving superconductivity [59]. Doped by intercalations was an efficient way to increase electron concentration [125–127]. In bulk MoS_2, when the metals were inserted into the adjacent MoS_2 layers, the intercalation would donate the electrons to MoS_2 and make the system metallic [128]. When MoS_2 was intercalated with calcium and strontium, the Ca_xMoS_2 and Sr_xMoS_2 compounds started to superconduct at ~4 K and 5.6 K [125]. In the intercalated and metallic $Rb_{0.3}MoS_2$, superconductivity was discovered with a maximum T_c ~6.9 K [127]. However, doped by intercalation would cause structural modifications in the material and therefore might affect its electronic band structure.

Recently, TMDs based field effect transistors (FET) with a gate dielectric made of ionic liquid, LaF_3 or $KClO_4$/polyethylene glycol became a very promising technique, because this gate dielectric could be regarded as the nanometer-scale capacitor and potentially give rise to a giant capacitance [129–131].

When a voltage was applied to the electrolyte, the electron would accumulate at the surface and the density would become very large. For the MoS_2, $MoSe_2$, WS_2 and $MoTe_2$ the densities could be closed to or larger than 10^{14} cm^{-1} [119,128,129]. Upon cooling, electrical transportation indicated that the samples exhibited metallic behavior with the surface resistivity decreasing dramatically. For example, in WS_2, the decrease in resistance was observed with an onset at ~4 K and the resistance reached zero at T_c ~0.5 K (critical temperature), as shown in Figure 4c [119]. As we know, the application of a perpendicular magnetic field B would destruct the zero-resistance state. The inset of Figure 4c shows the magnetic field dependence of the square resistance at T = 0.25 K, which indicated that the WS_2 reached the normal state value with magnetic field B ~0.14 T (critical magnetic field B_c) [119]. As for MoS_2, the electric-field-induced superconductivity was observed at T_c ~9.4 K, and the magnetic field of 3T broke the superconducting transition [128]. Shi et al. also studied the superconductivity of $MoSe_2$, $MoTe_2$ and WS_2; their results indicated that the T_c was ~7.1 K, 2.8 K and 8.6 K, respectively [129]. To investigate the dependence of superconductivity on thickness, Costanzo et al. studied the evolution of gate-induced superconductivity in exfoliated MoS_2 multilayers ranging from bulk-like to individual monolayers [132]. When the thickness was reduced from six to two layer, T_c and B_c decreased slowly. On reducing the thickness to monolayer, T_c and B_c were unambiguously suppressed as compared to all thicker multilayers. T_c jumped from approximately 7 K to 2 K and B_c became more than one order of magnitude smaller when passing from bilayer to monolayer MoS_2. The suppression of superconductivity in thinner sample might be caused by the fact that the fluctuations (thermal and quantum) responsible for the suppression of the long-range superconducting order became more important.

Intrinsic superconductivity in the 1T MoS_2 phase without electron injection was also investigated recently [133]. From the magnetic and electrical measurements, the superconductivity of 1T-MoS_2 crystals was observed under 4 K, and the zero temperature upper critical magnetic field of 1T-MoS_2 is estimated to be 5.02 T.

3. Preparation

Great efforts have recently been devoted to the preparation of low-dimensional TMDs, the details of which are as follows:

3.1. Mechanical Cleavage Method

Mechanical cleavage method is a traditional way to obtain few-layer or monolayer TMDs [30,31]. In 2004, Novoselov's group prepared graphene from highly-oriented pyrolytic graphite by using the mechanical cleavage method [1]. They also extended this method to other layered materials like BN, MoS_2, $NbSe_2$, $Bi_2Sr_2CaCu_2O_x$, and so on [30]. Just like drawing on a blackboard with chalk, the typical procedure of this method entails rubbing a fresh surface of a layered crystal against a clean substrate, like SiO_2/Si substrate, leaving a variety of flakes attached to it. Examined under an optical microscope carefully, 2D samples with various layers including monolayer were observed, and the thickness of the as-exfoliated sample could be identified by optical contrast. To further determine the thickness, the Raman spectrometer, PL spectrometer, and AFM can also be used. The AFM image of as-exfoliated $NbSe_2$ is shown in Figure 5a [30]; the varying thickness of the samples is portrayed by different colors. The bright color corresponds to the thick sample and the dark color corresponds to the thin one. The mechanical cleavage method can also be implemented with the aid of the Scotch-tape [27]. The typical procedure was as follows: The Scotch-tape was initially pressed onto the bulk crystal lightly and then removed carefully at a small angle. After this step, many thick sheets remained on the Scotch tape. The thin 2D nanosheets were obtained on repeatedly folding and peeling of the Scotch tape with thick sheets. The obtained 2D thin nanosheets were then transferred onto the pre-cleaned substrate by pressing the Scotch-tape with as-exfoliated nanosheets onto the SiO_2/Si substrate. After a slight pressure with tweezers, the Scotch-tape was removed from the substrate slowly and as-exfoliated nanosheets with various thickness were left on the substrate.

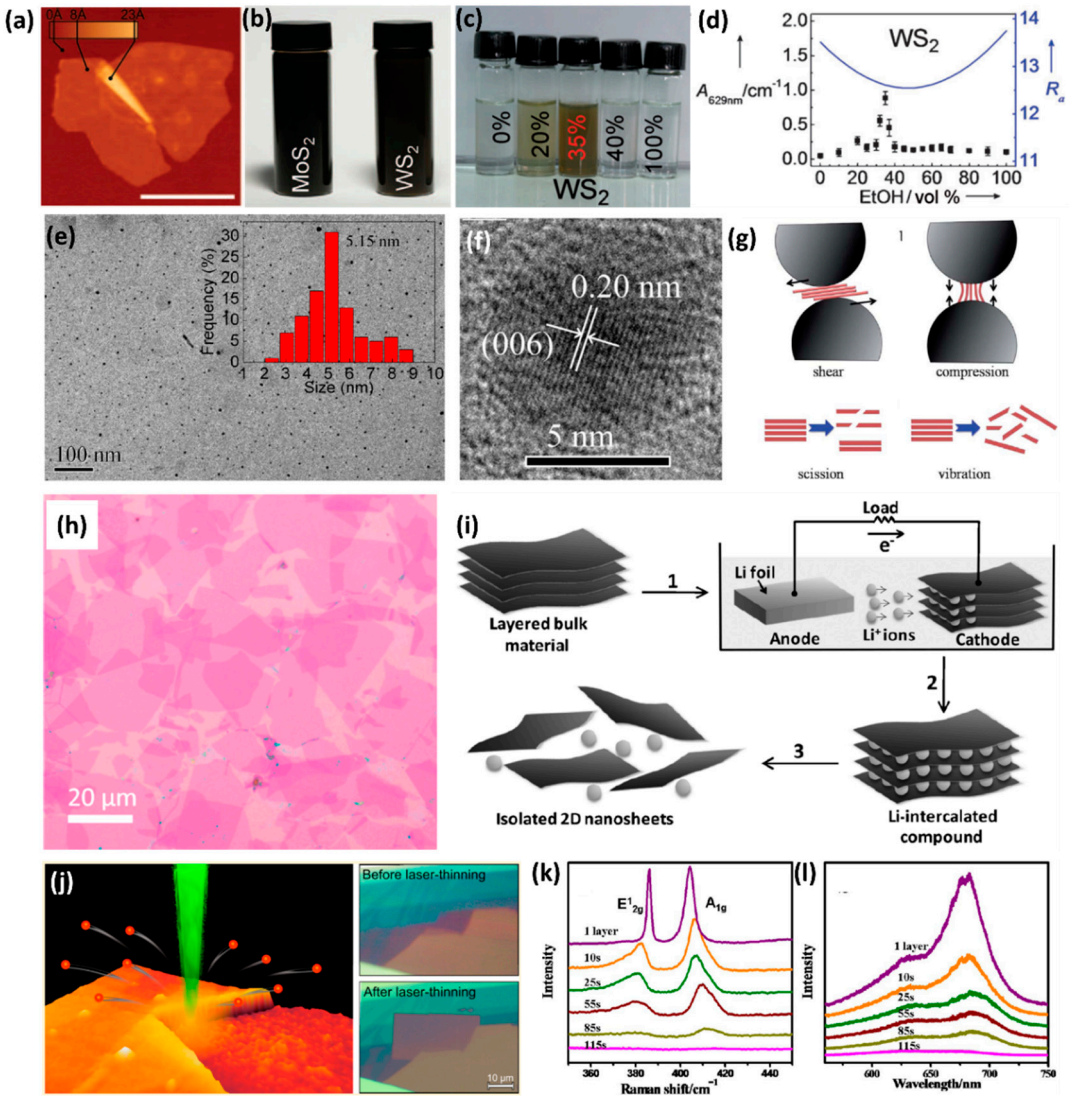

Figure 5. Top-down methods for the preparation of low-dimensional TMDs. (**a**) AFM image of as-exfoliated $NbSe_2$. The scale bar is 1 μm. The different brightness corresponded to different thickness [30]. (**b**) Photographs of the dispersions of MoS_2 and WS_2 in NMP [32]. (**c**) Photographs of WS_2 dispersions in various ethanol/water mixtures, which were stored for a week. The dispersion of WS_2 reached its maximum concentration in 35 vol.% ethanol/water [33]. (**d**) The calculated R_a values (solid line) and the absorbance (dots) of the WS_2 in various ethanol/water mixtures [33]. (**e**) Low-magnification TEM image of the MoS_2 QDs. The size distribution of the QDs was shown in the inset, which indicated that the size was in the range of 2–9 nm [29]. (**f**) High-resolution TEM images of a typical MoS_2 QDs. The clear lattice fringe indicated its highly crystalline structure [29]. (**g**) The illustration of shear and compression effects during the low-energy ball milling process, and the scission and vibration effects during the sonication process. The shear force induced exfoliation and the compression force induced exfoliation (**top**). Sonication induced scission and vibration induced exfoliation (**down**) [134]. (**h**) Optical image of the exfoliated monolayer TaS_2 on SiO_2/Si substrate. The size ranged from several tens of micrometers to more than 100 μm [135]. (**i**) Schematic drawing of the electrochemical lithiation process for the fabrication of 2D nanosheets from bulk material [36]. (**j**) **Left**: schematic illustration of the laser induced thinning method to prepare monolayer MoS_2. **Right**: optical image of a multilayer MoS_2 flake before and after scanned by a laser. The regions with different colors corresponded to different number of layers. After the laser-thinning process, the optical contrast of the rectangle region was uniform, consistent with that of a single MoS_2 monolayer [37]. (**k**,**l**) Raman

and PL spectra of monolayer MoS_2 after Ar^+ plasma irradiation with different time. On increasing the irradiation from 10 to 85 s, the Raman peaks became weak and broadened, and the PL intensities became much weaker. After 115 s irradiation, the Raman and PL peaks disappeared [38]. Reproduced with permission from [29]. Copyright AIP Publishing LLC, 2015. Reproduced with permission from [30]. Copyright Proceedings of the National Academy of Sciences of the United States of America, 2005. Reproduced with permission from [32]. Copyright American Association for the Advancement of Science, 2011. Reproduced with permission from [33,36]. Copyright Wiley-VCH Verlag GmbH & Co. KGaA, Weinheim, 2011. Reproduced with permission from [37]. Copyright American Chemical Society, 2012. Reproduced with permission from [38]. Copyright American Chemical Society, 2013. Reproduced with permission from [134]. Copyright The Royal Society of Chemistry, 2012. Reproduced with permission from [135]. Copyright American Chemical Society, 2017.

Mechanical cleavage method is the most convenient method to prepare the 2D layered TMDs. However, the yield of the as-prepared sample is very low, which can just meet the needs of laboratory research and hinder large-scale applications.

3.2. Liquid Exfoliation Method

Coleman et al. successfully exfoliated the layered materials by using the solvent-based method [32]. It was suggested that a successful solvent should meet two criteria. The first one is that the material must be suspended or dispersed in it for a reasonable amount of time. The second one is that the dispersed material must be highly exfoliated. Many common solvents have been experimented with in a bid to exfoliate the layered materials by sonication and centrifugation. The results indicated that surface tension of the solvents played a key role in the process. When the surface tension of the solvent matched with that of the layered material, it shows the best exfoliation and dispersity properties. For example, good dispersion of MoS_2 and WS_2 occurred for solvents with surface tensions in the range of 30–40 mJ/m^2. Figure 5b shows that the dispersions of MoS_2 (with the concentration of 0.3 mg/mL) and WS_2 (with the concentration of 0.15 mg/mL) in NMP are stable over a period of hundreds of hours [32]. Besides NMP, commonly used solvents like water and ethanol can also be used to exfoliate the layered TMDs. Zhou et al. tried water, ethanol and ethanol/water mixtures as solvents to disperse MoS_2 and WS_2 [33]. Their findings indicate that MoS_2 and WS_2 could hardly be dispersed in pure ethanol or water, while ethanol/water mixtures with different compositions exhibited significantly different dispersion properties. The 35% volume fraction (35 vol.%) of ethanol in water, especially, represents the highest dispersion concentration of WS_2 with 0.032 ± 0.003 mg/mL, and the suspensions could be stored for a week under ambient conditions (Figure 5c) [33]. In accordance with the theory of Hansen solubility parameters (HSP), the level of adaptation between the solvent and solute can be evaluated by the HSP distance R_a. The smaller the R_a is, the better the solubility will be (Figure 5d) [33]. Theoretical calculations indicated that the 35 vol.% ethanol–water mixture had the minimum value of R_a, which agreed well with the results observed in the experiment.

Gerchman et al. also tried an aqueous solution with surfactant as the solvent to exfoliate and suspend the WSe_2 [136]. To prepare the exfoliation solvent, anionic surfactant sodium dodecyl sulfate (SDS) was mixed with deionized water at a concentration of 2 g/L. They found that the surfactant system resulted in the highest concentration after sonication and centrifugation as compared to the pure solvents and solvent mixtures, such as acetone, NMP, 60% ethanol in water and 30% propan-2-ol in water. The high concentration was mainly caused by the fact that the surfactant could create a bond with the newly exposed surface of the WSe_2, so that each newly exfoliated layer could sterically and electrostatically be separated and stabilized. Moreover, the SDS solution could also stabilize the as-exfoliated suspension without noticeable precipitation after long periods of time.

Furthermore, liquid exfoliation technique could also be used to prepare TMDs QDs [29,94,137–139]. Typically, commercial TMDs microcrystals are firstly dispersed in a solvent, such as mixture of ethanol and water, 1 methyl-2-pyrrolidone or DMF. After sonication (with bath sonication and probe sonication) and centrifugation, the supernatant with QDs was obtained. Figure 5e shows the TEM image of the

MoS_2 QDs [29]. Statistical size distribution indicated that the size was in the range of 2–9 nm and the most probable size is about 5.2 nm, as shown in Figure 5e [29]. The clear lattice fringe observed from the high-resolution TEM images implied that their highly crystalline structure was retained after the sonication treatment (Figure 5f) [29].

3.3. Low-Energy Ball Milling Assisted Method

The product concentration achieved by the liquid-phase exfoliation method as discussed in Section 3.2 is not enough for the scalable production of 2D nanosheets. In order to make the thinning process more efficient and scalable, Wong's group reported a combined low-energy ball milling and sonication procedure for thinning and exfoliation of layered materials on a large scale [134]. Primarily, initial powder such as MoS_2, was dispersed in 0.05 weight% surfactant sodium dodecyl sulfate (SDS)–water solutions. Then the dispersion was transferred to planetary mill and the low-energy ball milling process were carried out with rotation speed of 100 rpm. During the ball milling process, shear force and compression force were exerted on MoS_2. The shear force could cleave the layers along the layer surface and the compression force could peel off thin MoS_2 nanosheets from the edges as shown in Figure 5g [134]. After 12 h ball milling, the milled sample was taken out followed by centrifugation at 5000 rpm for 20 min to remove aggregates. Afterwards, 2 h sonication process with the power of 80 W was carried out to further exfoliate layered materials. The sonication process could induce scission, which can break larger crystallites into smaller crystallites. The sonication process could also induce vibration, which could chip off the thin 2D nanosheets from the outer surfaces [134,140]. A schematic diagram is shown in Figure 5g [134]. After low-energy ball milling and sonication, MoS_2 nanosheets with concentration of 0.8 mg/mL were obtained. The diameters of the initial MoS_2 ranged from 0.5 to 10 μm. After exfoliation, the size of MoS_2 nanosheets was in the range of 50 nm to 700 nm and thickness was in the range of 1.2 nm to 8 nm.

3.4. Li-Intercalation Exfoliation Method

Joensen et al. developed a Li-intercalation exfoliation method to prepare a few-layer or monolayer MoS_2 [35]. The typical procedure is as follows: Firstly, they soaked the 2H-MoS_2 powder in a solution of n-butyl lithium in hexane (1.6 M), and kept it in this state for at least 48 h. In the process, lithium was intercalated into the interlayer of MoS_2, forming Li_xMoS_2. The insertion of Li^+ ions expanded the interlayer distance, which weakened the van der Waals interactions between the adjacent layers. After lithium intercalation, the Li_xMoS_2 was washed repeatedly with hexane, and then immersed in water. During the immersion process, the reaction between lithium and water generated H_2 gas, which made the MoS_2 layers go further apart from each other. With the aid of sonication, the final 2D MoS_2 dispersion liquid was obtained [35].

Recently, with the modified method, Wu's group prepared very-large-sized TMDs monolayers from fast exfoliation by manual shaking [135]. Instead of powder, they trialed the exfoliation with pristine MX_2 (M = group IVB-VIB, X = S, Se) single crystals. The crystals mixed with 1.6 M n-BuLi in hexane was sealed in a quartz-lined autoclave and kept at 100 °C. By deliberately controlling the reaction time, Li_xMX_2 with different lithium contents was obtained and gigantic expansion (∼94%) in Li_xMX_2 single crystals was realized. The gigantic expansion enabled exfoliation with a gentle-driving force. By only manual shaking within several seconds, expanded Li_xMX_2 crystals were exfoliated into homogenetic monolayers of submillimeter scale sizes and high crystallinity. Figure 5h represents the characteristic optical images of the exfoliated TaS_2 monolayers with sizes ranging from several tens of micrometers to more than 100 μm [135]. DFT calculations indicated that the insertion of lithium into MX_2 would induce lattice distortions along the in-plane direction and change the lattice parameter. Study on 13 kinds of TMDs materials demonstrated that the lateral size of the as-exfoliated monolayer was largely determined by the lattice strain in the Li_xMX_2 crystals. The large compressive strains in the lithium-intercalated compounds led to a small-size monolayer sample.

Zhang's group developed an electrochemical Li-intercalation exfoliation method to prepare the few-layer or monolayer TMDs [36]. Figure 5i gives a schematic illustration of the electrochemical Li-intercalation process in a battery test system, in which the layered bulk material (MoS_2, WS_2, TiS_2, TaS_2, etc.) was used as the cathode, and the Li foil as anode [36]. During the discharge process, the lithium was intercalated into the interlayer of the layered bulk material. On completion of lithium insertion, the intercalated compound was sonicated in water or ethanol to exfoliate the 2D nanosheets.

3.5. Laser and Plasma-Induced Thinning Method

To exploit thickness-dependent properties, a decisive factor is to control the thickness of the TMDs. Steele's group developed a technique to controllably thin out the multilayered MoS_2 down to a monolayer by using laser [37]. A schematic diagram is shown in Figure 5j [37]. During the laser-thinning progress, the laser scanned point-by-point along the surface of the MoS_2 flakes. The dose of the laser could be determined by adjusting step size, exposure time, and the power of incident laser. After several trials, they found that a 400-nm step size with 0.1 s exposure time and 10 mW of incident power could effectively thin out MoS_2 flakes with thickness of 20 layers. Figure 5j shows the optical image of MoS_2 flake on SiO_2/Si substrate, before and after the laser-thinning respectively. After the laser-thinning process, the laser scanning area showed uniform optical contrast. AFM characterization indicated that the thickness of the scanning area was 0.9 ± 0.3 nm, consistent with the thickness of monolayer MoS_2. Compared with monolayer MoS_2 prepared by mechanical cleavage method, the as-thinned monolayer sample showed similar semiconducting properties, which were confirmed by the PL, Raman vibration and electronic transport characterizations.

Ni's group demonstrated that Ar^+ plasma irradiation was also an effective way to regulate the thickness of MoS_2 [38]. The power and pressure of Ar^+ plasma were chosen as 50 W and 40 Pa, respectively. By increasing the irradiation time from 10 s to 85 s, the Raman and PL peaks of monolayer MoS_2 became weaker and broader, which indicated that the structure of MoS_2 became disordered. When the irradiation time was up to 115 s, the Raman and PL peaks disappeared, which demonstrated that MoS_2 layer was totally removed (Figure 5k,l) [38]. At the same time, they also conducted Ar^+ plasma irradiation on bilayer MoS_2. When the irradiation time was increased from 0 s to 115 s, the E^1_{2g} and A_{1g} peaks gradually shifted to the frequency of the monolayer MoS_2. As for the PL spectra, the PL intensity had an abrupt increase after 115 s irradiation, which indicated that the top layer has been totally removed, and the MoS_2 has transformed from bilayer to monolayer.

3.6. Thermal Annealing Method

Besides the laser and plasma-induced thinning method, thermal annealing in a controlled atmosphere can also be used to thin TMDs [141,142]. Taking MoS_2 as an example, the typical procedure is as follows: At first, scotch tape was used to exfoliate few-layer MoS_2 flakes from its bulk form and the as-exfoliated flakes were transferred to SiO_2/Si substrate subsequently. To conduct the thermal annealing process, the samples with silicon substrate were placed at the center of the CVD quartz tube. During annealing temperature, pressure and argon gas flow rate were set to 650 °C, 10 Torr and 5 sccm, respectively. It was discovered that one layer was lost after one hour of annealing. By increasing the annealing time, few-layer MoS_2 flakes could be peeled off layer by layer, which was confirmed by microspectrophotometry, Raman spectroscopy and AFM characterization. At the same time, the surface area showed a shrinkage during the annealing process, which indicated that sublimation occurred perpendicularly on the surface and along the surface, simultaneously. However, in repeated experiments, most atomically thin MoS_2 flakes appeared as inhomogeneous surfaces, which might be caused by vacancy defects. During annealing, vacancies could form randomly in any area because of sublimation and the vacancies could make their surrounding parts easier to sublimate due to broken covalent bonds.

3.7. Solid-Phase Reaction Method

Bottom-up chemical methods offer potentially powerful alternative exfoliation routes for preparing TMD nanosheets. Among the various ways to prepare TMDs, the solid-phase reaction method provides easier operation with good repeatability. During the synthesis, the transition metal and chalcogen powders were chosen as the precursors [143]. For the synthesis of 2D MoS_2 flakes, the molybdenum powder and sulphur powder were mixed in a stoichiometric ratio and loaded in a pre-cleaned quartz tube. After purging the quartz tube with ultrahigh-purity argon, the quartz tube with precursors was sealed. Then the sealed quartz tube was heated to 1000 °C at a rate of 15 °C/min and kept at 1000 °C for 3 days. After cooling to room temperature naturally, 2D MoS_2 flakes were obtained. The typical SEM image of the as-synthesized MoS_2 flakes is shown in Figure 6a. The lateral size of MoS_2 flakes could be up to 10 μm, and the thickness was about a few hundred nanometers. At the same time, by mixing the molybdenum (tungsten), sulphur and selenium powders in a stoichiometric ratio, $MS_{2(1-x)}Se_{2x}$ (M = Mo, W) alloys with different ratio of S and Se were achieved [143].

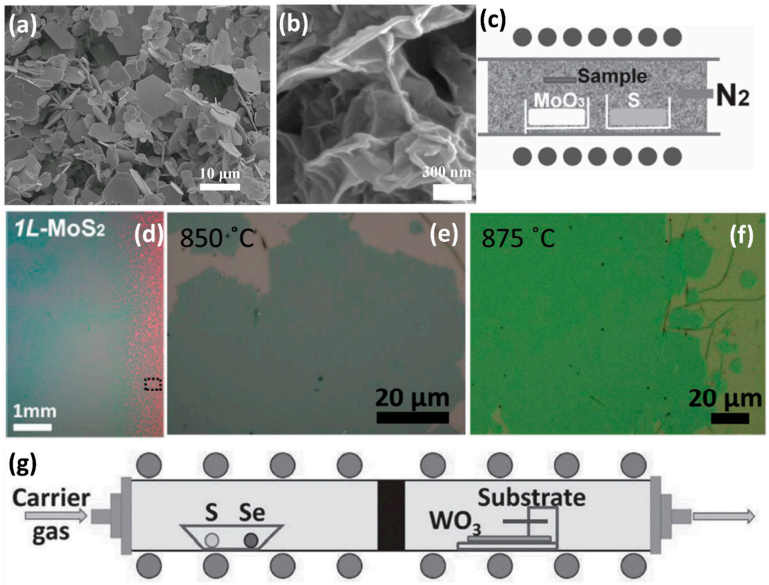

Figure 6. Bottom-up approaches (solid-phase reaction method, hydrothermal method and CVD method) for the preparation of 2D TMDs. (**a**) SEM image of MoS_2 flakes synthesized by solid-phase reaction method. The lateral size of MoS_2 flakes could be up to 10 μm, and the thickness was about a few hundred nanometers [143]. (**b**) SEM image of MoS_2 nanosheets synthesized by the hydrothermal method. The 2D MoS_2 nanosheets were rolled up and formed a nanoflower morphology [39]. (**c**) Schematic illustration of the setup for the synthesis of monolayer MoS_2. The substrates were placed face-down above the ceramic boat, which was filled with MoO_3. Another ceramic boat filled with S powder was located in the upstream of MoO_3 [41]. (**d**) Optical image of monolayer MoS_2. The MoS_2 showed a uniform morphology with centimeter sizes [42]. (**e**,**f**) Optical images of monolayer WSe_2 synthesized at different growth temperatures by CVD method. The monolayer WSe_2 exhibited the uniform morphologies with several tens microns in size [43]. (**g**) Schematic depiction of the growth setup for the synthesis of monolayer $WS_{2(1-x)}Se_{2x}$ alloys. The growth was conducted in a two-temperature zone tube furnace, where S and Se powders were placed in the upstream zone, and the WO_3 was placed in the downstream zone [108].Reproduced with permission from [39]. Copyright Macmillan Publishers Limited, 2014. Reproduced with permission from [41]. Copyright Wiley-VCH Verlag GmbH & Co. KGaA, Weinheim, 2012. Reproduced with permission from [42]. Copyright American Chemical Society, 2013. Reproduced with permission from [43]. Copyright The Royal Society of Chemistry, 2015. Reproduced with permission from [108]. Copyright Wiley-VCH Verlag GmbH & Co. KGaA, Weinheim, 2015. Reproduced with permission from [143]. Copyright Elsevier B.V., 2017.

3.8. Hydrothermal Method

Hydrothermal method is also an effective way to synthesis 2D TMD nanosheets. Our group synthesized MoS_2 nanosheets by using MoO_3 and KSCN as the reactants [39]. MoO_3 and KSCN with the molar ratio of 1:3 were dissolved in 80 mL distilled water. Subsequently, 0.28 mL HCl at a concentration of 12.5 mol/L was added into the reaction solution under violent stirring. Then the as-prepared solution was transferred into a 100 mL Teflon-lined stainless autoclave. After sealing tightly, the autoclave was heated in the oven at 240 °C for 24 h. The autoclave was then allowed to cool down at room temperature naturally. The reaction product was filtered off, washed with distilled water and absolute ethanol, and then dried in vacuum at 60 °C for 6 h. The morphology of the as-synthesized MoS_2 nanosheets was characterized by SEM, which showed that the 2D MoS_2 nanosheets rolled up, thus forming a nanoflower morphology (Figure 6b) [39].

Besides the MoO_3 and KSCN, $(NH_4)_2MoS_4$ could also be a precursor for the synthesis of MoS_2 nanosheets via hydrothermal method [144]. By adjusting the growth temperature and time at 220 °C and 12 h, respectively, Wang et al. also synthesized the MoS_2 nanosheets with different diameters. They also integrated 2D MoS_2 nanosheets with drug delivering implant for highly-efficient near infra-red triggered synergistic tumor hyperthermia. The details can be found in Section 4.5.

At the same time, hydrothermal method can also be used to prepare TMDs QDs [40,145–147]. Wang et al. synthesized MoS_2 QDs by using $Na_2MoO_4{\cdot}2H_2O$ and L-cysteine as the precursors [147]. In brief, the $Na_2MoO_4{\cdot}2H_2O$ was primarily dissolved in water, and then the solution was adjusted to pH 6.5 with HCl. Afterwards, the L-cysteine and water were added to the above solution followed by the ultrasonication process. Then the mixture was transferred into autoclave and reacted at 200 °C for 36 h. After centrifugation, the supernatant containing MoS_2 QDs were obtained. Furthermore, the hydrothermal process is also beneficial to the cutting of the basal plane when preparing TMDs QDs. Taking MoS_2 QDs as an example, the short time ultrasound treatment of MoS_2 nanosheets with subsequent hydrothermal process produced MoS_2 QDs with a size distribution of ~2.0 $\pm$ 0.5 nm in diameter [141].

3.9. CVD Method

The lateral size of the 2D TMDs synthesized by the aforementioned methods is very small, an order of several micrometers, which hampers industrial applications in the future. Therefore, the methods for preparing 2D TMDs by the CVD method are of wide concern. In general, when the CVD method is adopted to synthesize few-layer or monolayer TMDs, the products are always grown on SiO_2/Si substrates, sapphire, Au foils or quartz substrates by using transition metal oxide (MO_3) and chalcogen (X) powders as precursors [41–44,148–150]. For example, monolayer MoS_2 was grown on SiO_2/Si substrate in a quartz tube furnace at atmospheric pressure by using N_2 or Ar gas as the carrier gas. Figure 6c shows a schematic illustration of the experimental setup [41]. The S powder was located at the upstream of the tube, while the MoO_3 powder with the substrate placed face-down above was placed at the downstream of the quartz tube. Prior to growth, the SiO_2/Si substrates were treated by graphene-like molecules, such as reduced graphene oxide (rGO), perylene-3,4,9,10-tetracarboxylic acid tetrapotassium salt (PTAS) and perylene-3,4,9,10-tetracarboxylic dianhydride (PTCDA), which could promote surface nucleation efficiency and layer growth [41,42]. During the growth process, the MoO_3 powder was firstly reduced by sulfur vapor to form volatile sub-oxide MoO_{3-x} [35,36]. Then the MoO_{3-x} molecule was further reacted with sulfur vapor to form monolayer MoS_2 on the substrates [35,36]. Figure 6d shows the optical image of the uniform MoS_2 monolayers with several centimeters in size, which are grown on a SiO_2/Si substrate [42]. By using varying growth parameters, the transition between vertical and horizontal growth was achieved [151,152].

The chemical reactivity of Se is much lower than that of S [107,153]. As a consequence, compared with transition metal disulfides, transitional metal diselenium compounds like WSe_2 and $MoSe_2$ were difficult to synthesize. Our group successfully synthesized the monolayer WSe_2 by using a mixture of argon–hydrogen (5%) gas as the carrier and reduction gas [43]. With the introduction of

H_2, the reduction of WO_3 to WO_{3-x} became much easier, facilitating subsequent reactions. During the synthesis process, we initially heated the furnace to 925 °C, then conducted a sub-cooling step to a lower temperature and maintained the lower temperature for 15 min. This lower temperature was very important for the growth of monolayer WSe_2. Figure 6e,f show the optical images of as-synthesized WSe_2 at different growth temperatures, which exhibit uniform morphologies with several tens microns in size [43]. AFM, Raman and PL characterizations confirmed the monolayer configuration in the as-grown WSe_2. By optimizing the synthesis conditions, we also synthesized the monolayer $WS_{2(1-x)}Se_{2x}$ alloys with different Se contents [108,109]. Figure 6g shows a schematic illustration of the growth setup. In the upstream of the furnace, the ceramic boat loaded two reactants, the S powder and Se powder. Meanwhile, the WO_3 powder was evenly spread on a quartz holder located in the downstream. We also performed atomic-scale analysis of the $WS_{2(1-x)}Se_{2x}$ alloys by using the HRSTEM, details of which are provided in Section 2.1.

During the growth of TMDs by CVD method, mass flux and growth rate played a key role in the morphology of the TMDs, where mass flux determined the amount of metal precursors involved in the formation of the nucleus and the growth of domains, and the growth rate dominated the grain size [154]. Many transition metals or metal oxides have high melting points and low vapor pressure, which lead to very low mass flux and limited reaction [154]. Therefore, many of the layered TMDs are difficult to produce via the CVD method. Inspired by the fact that the molten-salt could be used to produce ceramic powders at relatively low temperature, Zhou et al. demonstrated that molten-salt-assisted CVD could be broadly applied for the synthesis of a wide variety of TMDs in atomically thin, including 32 binary compounds, 13 alloys and two heterostructured compounds [154]. Thermogravimetry and differential scanning calorimetry measurements indicated that the melting points of salts mixed with the metal sources fell in the range of 600 °C to 850 °C. The molten salts reduced the melting points of the metal precursors or formed oxychlorides via reaction with some metal oxides so as to increase the mass flux and the rate of the reaction. The universal method for the synthesis of 2D TMDs facilitated the exploration of their physical properties and applications.

For real applications, the controlled growth of large-area uniform monolayer TMDs on low cost substrates is very important. Very recently, Zhang's group realized the direct synthesis of a 6-inch uniform monolayer MoS_2 on solid soda-lime glass through a face-to-face metal-precursor supply route in a facile CVD process [155]. Experimental study demonstrated that the continuous 6-inch monolayer MoS_2 film was synthesized at the edge growth rate of around 1.2 μm/s. This growth rate was much faster than that on common insulating substrates, such as SiO_2/Si (0.4 μm/s) and sapphire (0.2 μm/s). This high growth efficiency was proven to be facilitated by uniformly distributed Na in soda-lime glass, which served as perfect catalysts for rapid and large-scale uniform growth. DFT calculations indicated that Na adsorption could reduce the energy barriers for MoS_2 growth along the S-terminated edges and Mo-terminated edges, which agreed well with the experimental results.

Xu et al. also successfully synthesized the one-dimensional $WS_{2(1-x)}Se_{2x}$ nanotubes via the selenization and sulfurization process [45]. The carbon fibers (CFs) with wonderful electric conductivity, high thermal and chemical stabilities were chosen as the substrate in their synthesis. Firstly, WO_3 nanowires were synthesized by a catalyst-free physical vapor deposition method. The WO_3 powder, which evaporated at high temperature deposited on the CFs, showed the nanowires morphology at a vacuum lower than 1 Pa at inert atmosphere. CFs with large coverage of WO_3 nanowires were then placed in a tube furnace and S and Se powders were chosen as the precursors to transfer the WO_3 nanowires into $WS_{2(1-x)}Se_{2x}$ nanotubes. Figure 7a,b show the typical SEM images of the WO_3 nanowires and $WS_{2(1-x)}Se_{2x}$ nanotubes, respectively. The entire surfaces of the CFs were vertically and uniformly covered with high-density $WS_{2(1-x)}Se_{2x}$ nanotubes. The HRTEM characterization (Figure 7c) indicated that the as-synthesized one-dimensional $WS_{2(1-x)}Se_{2x}$ sample, showing multiwall nanotubes morphology. CVD method can also be used to prepare the 1D MoS_2 nanobelts [49,80]. Recently, our group successfully synthesized one-dimensional MoS_2 nanobelts by using n-type silicon as the substrate [80]. Figure 7d shows the optical image of the MoS_2 nanobelts. The length was about

10–20 μm, and the area coverage was around 5%. As discussed in Section 2.1, the (001) basal planes of the MoS_2 nanobelt were standing vertically on the substrate and the edges of the base planes formed the top surfaces of the nanobelt [90]. We also realized the control of its chemical and physical properties by forming $MoS_{2(1-x)}Se_{2x}$ nanobelts alloys through optimization of growth conditions [156].

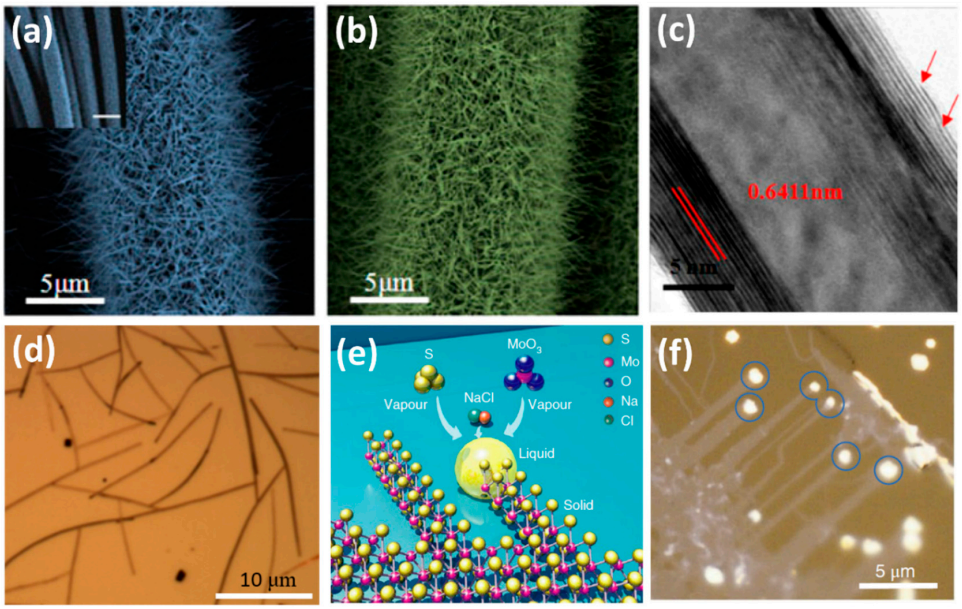

Figure 7. CVD synthesis of 1D TMDs. (**a**,**b**) SEM images of WO_3 nanowires and $WS_{2(1-x)}Se_{2x}$ nanotubes, respectively. The entire surfaces of the CFs were covered vertically and uniformly with high-density WO_3 nanowires and $WS_{2(1-x)}Se_{2x}$ nanotubes. The WO_3 nanowires showed the length of ~5 μm and the diameter of ~100 nm [45]. (**c**) HRTEM image of $WS_{2(1-x)}Se_{2x}$ nanotubes. The spacing of $WS_{2(1-x)}Se_{2x}$ nanotubes between lattice fringes was 0.6411 nm [45]. (**d**) Optical image of MoS_2 nanobelts. The area coverage was around 5%, and the length was 10~20 μm [80]. (**e**) Schematic illustration of the growth of MoS_2 narrow ribbons. Firstly, the liquid phase Na–Mo–O in small droplets was formed. Then the Na–Mo–O droplet dissolved sulfur. At last, the ribbons grew horizontally and the droplet crawled laterally [50]. (**f**) Optical image of MoS_2 ribbons grown on a NaCl crystal. The ribbons showed the widths of a few tens of nanometers to a few micrometers and lengths ranged from a few to tens of micrometers [50]. Reproduced with permission from [45]. Copyright American Chemical Society, 2014. Reproduced with permission from [50]. Copyright Macmillan Publishers Limited, 2018. Reproduced with permission from [80]. Copyright American Chemical Society, 2015.

With the aid of alkali metal halide, the highly crystalline monolayer MoS_2 ribbons with a width of few tens to thousands of nanometers were also successfully synthesized [50]. During this growth, the MoO_3 reacted with NaCl and formed the molten Na–Mo–O droplets. These droplets crawled on the substrate surface and mediated the highly anisotropic growth of MoS_2 ribbons when saturated with sulfur. With the lateral displacement of the droplet, the horizontal growth of ribbons kept going. The schematic illustration is shown in Figure 7e [50]. Figure 7f shows the optical image of MoS_2 ribbons grown on a NaCl crystal substrate [50]. Differing from the typical triangular morphology, ribbons with lengths from a few to tens of micrometers, and widths of a few tens of nanometers to a few micrometers were grown. The bright dots indicated by the circles were characteristic features of nanostructures that resulted from the crawling mode.

3.10. Annealing of the $(NH_4)_2MoS_4$ Precursor

Besides the transition metal oxide (MO_3), other compounds like ammonium thiomolybdate ($(NH_4)_2MoS_4$) can also be reactants during the synthesis of few-layer TMDs. Liu et al. reported the

successful synthesis of large area MoS_2 thin sheets on a variety of insulating substrates by the thermal decomposition of $(NH_4)_2MoS_4$ in the presence of sulfur vapor [51]. The schematic illustration is shown in Figure 8a [51]. Firstly, the $(NH_4)_2MoS_4$ was dip-coated on SiO_2/Si or sapphire substrates. Then, a two-step annealing processes were carried out to transfer the $(NH_4)_2MoS_4$ into MoS_2 films. The first annealing process was carried out at a low pressure (1 Torr) in an Ar/H_2 atmosphere (flow rate 4:1) to efficiently remove the residual solvent, NH_3 molecules, and other byproducts dissociated from the precursors. Compared with the annealing temperature of 500 °C in the first annealing process, the high-temperature annealing at 1000 °C in Ar or Ar + S atmosphere was used to improve the MoS_2 crystal structure. The electrical properties of transistor devices fabricated with as-prepared MoS_2 thin layers were comparable with that of mechanically exfoliated MoS_2.

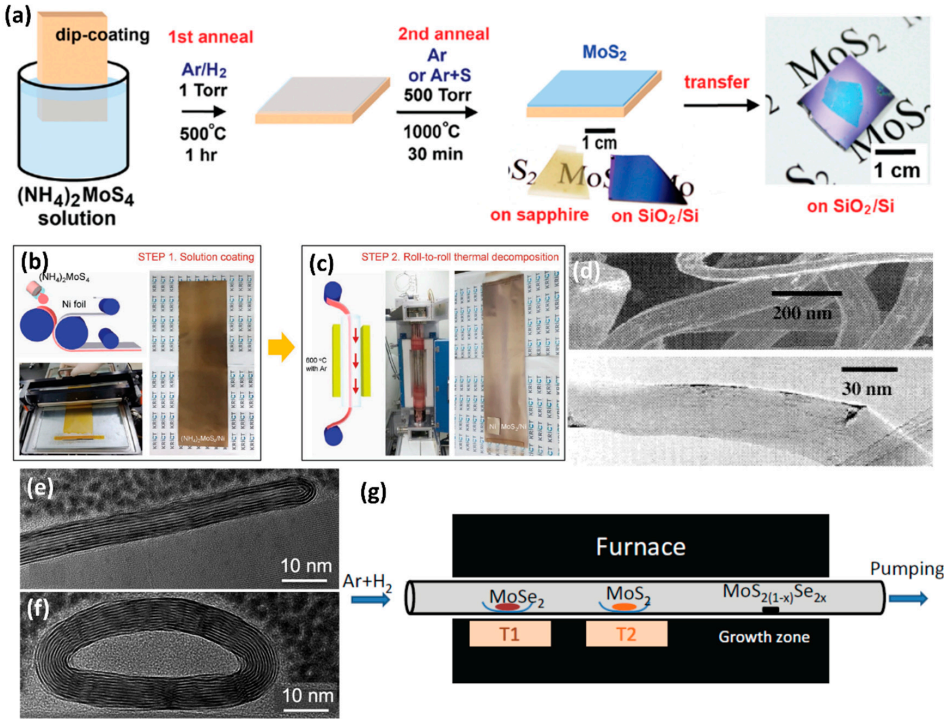

Figure 8. Bottom-up approaches (annealing of the $(NH_4)_2MoS_4$ precursor, chemical vapor transport method and physical vapor deposition method) for the preparation of low-dimensional TMDs. (**a**) Schematic depiction of the two-step thermolysis process for the synthesis of MoS_2 thin layers. The insulating substrate was immersed into the $(NH_4)_2MoS_4$ solution followed by the two-step annealing process [51]. (**b**,**c**) Photographs and schematic illustration of coating of $(NH_4)_2MoS_4$ on Ni foils and roll-to-roll thermal decomposition for layer-controlled MoS_2 on Ni foils [157]. (**d**) SEM (**top**) and TEM (**down**) images of MoS_2 nanotubes. The MoS_2 nanotube had a typical length of several hundreds of nanometers and a uniform diameter about 50 nm [158]. (**e**) Typical TEM image of MoS_2 nanoribbon. At the edge of the nanoribbon, it showed the wrapping of the layers [54]. (**f**) Cross-section TEM image of MoS_2 nanotubes. The nanotubes had minor and major radii of 5 nm and 20 nm, respectively [54]. (**g**) Schematic illustration of three-zone furnace for the physical vapor deposition growth of monolayer $MoS_{2(1-x)}Se_{2x}$. $MoSe_2$ and MoS_2 powders were put in the first and second upstream zones, respectively, and the substrate was put in the third zone. During the growth, the temperature of the third zone was ~600–700 °C, which was higher than that of the first and second zones (940–975 °C) [48]. Reproduced with permission from [48]. Copyright Wiley-VCH Verlag GmbH & Co. KGaA, Weinheim, 2014. Reproduced with permission from [51]. Copyright American Chemical Society, 2012. Reproduced with permission from [54]. Copyright AIP Publishing LLC, 2015. Reproduced with permission from [157]. Copyright Wiley-VCH Verlag GmbH & Co. KGaA, Weinheim, 2017. Reproduced with permission from [158]. Copyright American Chemical Society, 2001.

To trigger actual industrial applications, Lim et al. developed a facile method for the large-scale production of MoS_2 layers by using the roll-to-roll manufacturing technology [157]. During the synthesis, they chose inexpensive Ni foils as the substrate and achieved 50 cm long MoS_2 layers with excellent long-range uniformity and optimum stoichiometry. Initially, a $(NH_4)_2MoS_4$ solution in ethylene glycol was bar-coated onto a hydrophilic-treated 25 μm thick Ni foils by UV irradiation. The Ni foils were then placed in the roll-to-roll chamber and annealed with the introduction of N_2 under a certain vacuum. Figure 8b,c present the schematic illustration and photographs of simple coating of $(NH_4)_2MoS_4$ on Ni foils and roll-to-roll thermal decomposition of MoS_2 [157]. At the same time, they established the optimized conditions for the synthesis of layer-controlled MoS_2 by the precise control of the $(NH_4)_2MoS_4$ concentration. To evaluate the layer homogeneity of such large area MoS_2 samples, they performed Raman characterization at every 1 cm. Two typical Raman active modes (E^1_{2g} and A_{1g}) are observed over the entire area from all samples, which demonstrates that the synthesis yielded homogeneous MoS_2.

Annealing of $(NH_4)_2MoS_4$ with subsequent hydrogen treatment could effectively produce MoS_2 and WS_2 nanotubes [52,158]. For the preparation of MoS_2 nanotubes, $(NH_4)_2MoS_4$ was heated at 400 °C in an argon atmosphere, after which MoS_3 was obtained [52]. The reaction involved was:

$$(NH_4)_2MoS_4 \rightarrow MoS_3 + H_2S + NH_3$$

Heating the obtained amorphous MoS_3 in a stream of H_2 at 1200–1300 °C realized an excellent yield of nanotubes. To obtain WS_2 nanotubes, similar reactions could be carried out with ammonium thiotungstate as the precursor [52].

Chen et al. also successfully synthesized MoS_2 nanotubes by direct reaction of $(NH_4)_2MoS_4$ and hydrogen at a relatively low temperature [158]. At first, $(NH_4)_2MoS_4$ was pretreated by ball-milling under a hydrogen atmosphere for 1 h to "activate" the fine powders. Then, the active powder was sintered in a floating hydrogen/thiophene at a relatively low temperature of 400 °C. After 1 h growth, MoS_2 nanotubes with specific surface area of 58 m^2/g were obtained. As shown in Figure 8d, the as-synthesized MoS_2 nanotube had a typical length of several hundreds of nanometers and a uniform diameter of about 50 nm [158].

3.11. Chemical Vapor Transport Method

Chemical vapor transport method is a traditional technique for the preparation of nonvolatile solids and has been used to produce single crystals of TMDs. For the growth of TMDs crystals, the precursors and transport agents (iodine) were sealed in a quartz ampoule under high vacuum. The sealed ampoule was then heated under a temperature gradient in which the I_2 molecules could carry TMDs into the gas phase in the high temperature zone and release them at the cold end. To realize the direct growth of 2D TMDs, Hu et al. designed the experiments by modifying the reaction ampoule and tuning the growth parameters [53]. In the case of growing monolayer MoS_2, the MoO_3 and S were selected as precursors, and I_2 was selected as a transporting agent. By reducing the amounts of MoO_3 with S to about 1:1000–1:10,000 and I_2 to 1:10, dramatical decrease of the growth rate was achieved, and the monolayer MoS_2 was produced in fluorophlogopite mica at a growth temperature of 300–600 °C for 0.5–2 h. For example, with chemical vapor transport growth of 30–40 min at 400 °C, monolayer MoS_2 triangular flakes with a side length of 30–60 mm were obtained. Besides MoS_2, this method was also used in the growth of 2D WS_2, $MoSe_2$, $Mo_xW_{(1-x)}S_2$ alloys and ReS_2.

The chemical vapor transport could also be used to prepare TMDs nanotubes and nanoribbons with very slow rate [54,159]. For the preparation of MoS_2 nanotubes or nanoribbons, MoS_2 powder and iodine were sealed in silica ampoule at a pressure of 7×10^{-4} Pa. The iodine transported the evacuated MoS_2 vapor phase with the temperature from 1133 K to 1010 K with a temperature gradient of 6.2 K/cm in a two-zone furnace. After three weeks of growth, the silica ampoules were cooled to room temperature with a controlled cooling rate of 60 °C/h, and a few percent of the starting MoS_2

powder was transported by the reaction to form nanotubes. With continuous growth, some of the nanotubes would spontaneously collapse and form the ribbon shapes. The length of the nanotubes could be up to several millimeters in length, and the diameters in multiwall nanotubes ranged from several micrometers to less than ten nanometers. The typical TEM image of MoS_2 nanoribbon and cross-section TEM image of MoS_2 nanotubes is shown in Figure 8e,f [54]. At the nanoribbon edge, the layers have shown wrapping morphology, and the MoS_2 nanotubes with a layer thickness of 11 monolayers had minor and major radii of 5 nm and 20 nm, respectively.

3.12. Physical Vapor Deposition Method

Physical vapor deposition method is another efficient way to prepare 2D TMDs and their alloys [48,160,161]. Typically, the TMDs powder source was placed in the upstream of a horizontal quartz tube furnace and the cleaned substrate was placed downstream, far from the TMDs powder with a temperature gradient. By finely tuning the growth conditions, such as gradient of deposition temperature, evaporation temperature, gas flow, high-quality monolayer or few-layer TMDs were grown on substrate. For the growth of TMDs alloys, the difference was that two or more kinds of powder were placed in the upstream of a horizontal quartz tube furnace. By adjusting the molar ratio of the powder, different contents of transition metal or chalcogens were achieved in the 2D alloys. Figure 8g illustrated the setup used in the growth of the $MoS_{2(1-x)}Se_{2x}$ monolayer; $MoSe_2$ and MoS_2 powders were put in the first and second zones of the three-zone furnace, respectively.

4. Applications

4.1. Electronic Devices

According to Moore's Law, the increase of transistors integration in semiconductor chips will result in the channel length of the transistors being below 10 nm [162]. To maintain good gate control of the channel and to minimize leakage current, channel thickness below 2 nm is required [163–165]. This is extremely challenging for silicon because ultrathin silicon suffers from surface roughness effects. The surface roughness scattering will reduce its mobility by nearly two orders of magnitude [163–165]. Fortunately, the emergence of novel classes, such as 2D layered TMDs, which do not have surface roughness, has opened up new ways in device design [166]. In 2005, Geim's group initially investigated the electrical conductivity of mechanically cleaved 2D MoS_2 [30]. The measured mobilities ranged from 0.5 to 3 $cm^2 \cdot V^{-1} \cdot s^{-1}$, which agreed well with the value achieved in its bulk form. The low mobility of MoS_2 hampered its application in practical devices, which facilitated researchers to make great effects to improve its electrical performance. Jena et al. simulated the effect of dielectric engineering on the influence of carrier mobility in 2D and 1D semiconductor nanostructures [167]. Their results indicated that the scattering from Columbic impurities could be strongly damped when the nanostructures were coated with high-κ dielectrics. The damping of Columbic scattering improved the mobility of carriers, which made the nanostructures show better electrical behavior.

Inspired by their theoretical predictions, Kis's group chose HfO_2 as the high-κ dielectric and deposited it on the top surface of monolayer MoS_2 by an atomic layer deposition method [31]. Followed by the electron-beam lithography process, the monolayer MoS_2-based top-gated configuration device with HfO_2 as the gate dielectric was fabricated, as shown in Figure 9a [31]. The width of the top gate was 4 μm and the top gate length, source–gate and gate–drain spacing was 500 nm. Figure 9b shows the room-temperature transfer characteristic for the device with the bias voltage of 10 mV, from which the mobility of ~217 $cm^2 \cdot V^{-1} \cdot s^{-1}$ was extracted. The I_{ds}–V_{tg} curves with the bias voltage ranging from 10 mV to 500 mV in Figure 9c indicated that the room-temperature on/off ratio exceeded 10^8 and the subthreshold slope for the transition between the on and off states was 74 mV/dec for a bias V_{ds} of 500 mV. These values were comparable to the performance of thin silicon films. However, for the back-gated configuration, the monolayer devices displayed mobility of 0.1–10 $cm^2 \cdot V^{-1} \cdot s^{-1}$, much lower than the previously reported phonon-scattering-limited room-temperature mobility.

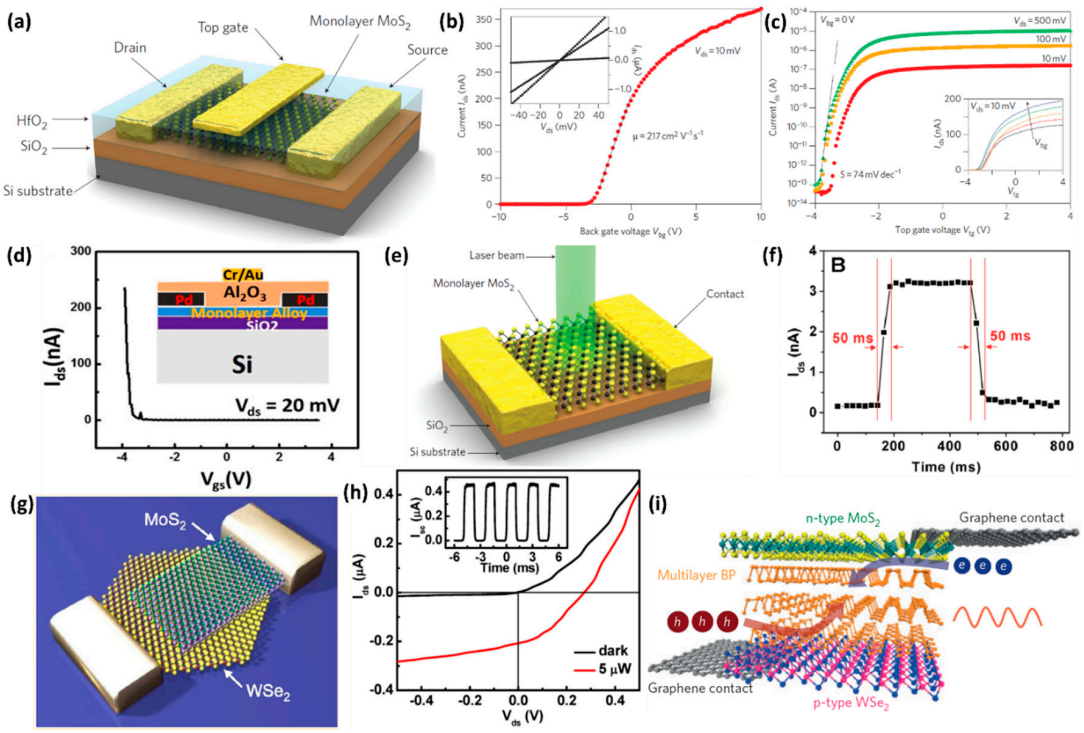

Figure 9. Application of low-dimensional TMDs in electronic devices and optoelectronic devices. (**a**) Schematic view of monolayer MoS_2 based transistors. 30 nm HfO_2 was chosen as the top gate dielectric because of its high dielectric constant of 25, band gap of 5.7 eV [31]. (**b**) Transfer characteristic of monolayer MoS_2 FET with the bias voltage V_{ds} of 10 mV, from which the channel mobility of ~217 $cm^2 \cdot V^{-1} \cdot s^{-1}$ was estimated. The inset showed the I_{ds}–V_{ds} curve acquired with V_{bg} values of 0, 1 and 5 V, which indicated that gold contacts were ohmic [31]. (**c**) I_{ds}–V_{tg} curves of the MoS_2 transistor with the bias voltage ranging from 10 mV to 500 mV. The measured current on/off ratio was higher than 1×10^8, and subthreshold slope for the transition between the on and off states was 74 mV/dec [31]. (**d**) Transfer characteristic of top-gated monolayer $WSe_{2(1-x)}S_{2x}$ (x = 0.28) device with the bias voltage V_{ds} of 10 mV. The insert shows the schematic view of the transistors with the top-gate electrode [43]. (**e**) Schematic view of the single-layer MoS_2 photodetector. During the measurement, the laser beam directly focused on the surface of MoS_2 [168]. (**f**) Photoswitching rate of single-layer MoS_2 phototransistor at V_{ds} = 1 V, P_{light} = 80 μW. The switching duration for the current rise or decay process was only ~50 ms [169]. (**g**) Schematic illustration of the WSe_2/MoS_2 vertical heterojunction device [170]. (**h**) The output curve of the WSe_2/MoS_2 heterojunction p-n diode with and without illumination. The output characteristics showed clear photovoltaic effect with an open-circuit voltage of ~0.27 V and a short-circuit current of ~0.22 μA. The inset showed temporal response of the photocurrent generation under 514 nm illumination (10 μW), from which the EQE was determined as the 11% [170]. (**i**) Schematic illustration of a 2D heterostructure LED. A multilayer BP thin film was sandwiched between the n-type MoS_2 and p-type WSe_2 which were used to inject the electrons and holes, respectively [171]. Reproduced with permission from [31]. Copyright Macmillan Publishers Limited, 2011. Reproduced with permission from [43]. Copyright IOP Publishing Ltd., 2016. Reproduced with permission from [168]. Copyright Macmillan Publishers Limited, 2013. Reproduced with permission from [169]. Copyright American Chemical Society, 2011. Reproduced with permission from [170]. Copyright American Chemical Society, 2014. Reproduced with permission from [171]. Copyright Macmillan Publishers Limited, 2014.

Lee et al. investigated the electrical properties of CVD growth TMDs [42]. Their results indicated that the on−off current ratio exceeds 10^7; the room temperature and low temperature mobilities were up to 1.2 $cm^2 \cdot V^{-1} \cdot s^{-1}$ and 500 $cm^2 \cdot V^{-1} \cdot s^{-1}$ respectively. These values were comparable to the

exfoliated monolayer MoS_2 fabricated without high κ-dielectrics screening. Our group also studied the electrical performance of as-grown monolayer WSe_2: the back gated configuration field-effect mobility was ~0.2 $cm^2 \cdot V^{-1} \cdot s^{-1}$ and the hole carrier concentration was ~1.11 × 10^{18} cm^{-3} [43]. This low field-effect mobility might be caused by the grain boundaries in the as-grown sample, which could scatter the carriers during transport. By partially substituting the Se atoms with S atoms in the monolayer WSe_2, we observed similar electrical behavior [109]. The calculated mobilities for the monolayer $WSe_{2(1-x)}S_{2x}$ with x = 0.07 and 0.85 were ~0.02 $cm^2 \cdot V^{-1} \cdot s^{-1}$,while for the $WSe_{2(1-x)}S_{2x}$ with x = 0.28, a much higher mobility of 0.2 $cm^2 \cdot V^{-1} \cdot s^{-1}$ was achieved. The mobility difference observed in the $WSe_{2(1-x)}S_{2x}$ alloys might be caused by the different defect densities in the as-grown samples as well as the contact issues. After we coated a layer of 20 nm Al_2O_3 on the surface of $WSe_{2(1-x)}S_{2x}$ (x = 0.28) as shown in Figure 9d [43], the top-gated device displayed mobility of ~46.5 $cm^2 \cdot V^{-1} \cdot s^{-1}$, two orders of magnitude higher than the back-gated one. Compared to the current prevailing III–V materials, 2D TMDs with low mobility may not be suitable for high-performance applications. However, large band gap and excellent electrostatic integrity make TMDs suitable for applications in low power related areas [172].

4.2. Optoelectronic Devices

The wide band gap (1.2–1.9 eV), especially monolayer direct band gap materials, makes TMDs suitable for applications in optoelectronic devices, because of their high absorption coefficient and efficient electron-hole pair generation [21,95,168]. Lopez-Sanchez et al. fabricated a phototransistor based on monolayer MoS_2 [168]. The schematic view of the photodetector is shown in Figure 9e; the focused laser beam is used to probe the device. The photodetector showed a photoresponse in the range of 400–680 nm and an ultrasensitive behavior with a maximum external photoresponsivity of 880 $A \cdot W^{-1}$ at a wavelength of 561 nm. The direct band gap in monolayer MoS_2 also resulted in ~9000 fold higher photoresponsivity in monolayer MoS_2 compared to that in multilayer devices. When the V_{ds} = 8 V and V_g = −70 V were applied, the photodevice showed a typical rise time and drop time of τ_{rise} = 4s and τ_{decay} = 9s, respectively. The slow switch between the On state and Off state might be influenced by the surroundings of the MoS_2 photodevice, like O_2/H_2O molecule adsorption [168,173]. The monolayer MoS_2 based photodetector fabricated by Zhang's group shows an excellent switching behavior [169]. Figure 9f shows the photoswitching rate test of photoswitching behavior at V_{ds} = 1 V, P_{light} = 80 μW. The observed switching duration for the current rise or decay process was only ~50 ms, much faster than the value reported by Lopez-Sanchez and co-workers [169]. However, the calculated photoresponsivity was very low—could only reach as high as 7.5 mA/W.

The p-n diodes composed of atomically thin TMDs were also realized. In general, the n-type materials referred to MoS_2, $MoSe_2$ or WS_2, and the p-type material referred to WSe_2. Cheng et al. fabricated WSe_2/MoS_2 heterojunction diodes by vertically stacking the synthetic WSe_2 and exfoliated MoS_2; a schematic illustration is depicted in Figure 9g [170]. They observed a clear photovoltaic effect with an open-circuit voltage of ~0.27 V and a short-circuit current of ~0.22 μA in the as prepared p-n diodes by measuring its output characteristics (Figure 9h). The external quantum efficiency (EQE) in the heterojunction could reach a maximum of 12% under a 514-nm laser excitation with a power of 0.5 μW. To further increase the EQE of the WSe_2/MoS_2 heterojunction diodes, Lee and co-workers prepared a graphene-sandwiched WSe_2/MoS_2 heterojunction diodes with different thicknesses [174]. The measured maximum EQE at 532 nm was 34%; this was mainly due to the fact that the graphene with high conductivity could reduce the interlayer recombination of the majority carriers and speed up the collection of the photo-generated carriers. However, the improved value was still inferior to that of materials used in the industry, such as Si, GaAs, CdTe or $CuIn_xGa_{(1-x)}Se_2$, which showed maximum value of >80% in the visible range [175–178]. The low EQE in TMDs based photovoltaic devices may be caused by defects and surface states, which are produced during the synthesis and layers' assembly, respectively. The defects or surface states fasten the carrier recombination or localize the carriers, so that the number of carriers collected by electrodes reduces greatly.

The heterojunction based on 2D TMDs could also be applied to the light emitting diode (LED). Figure 9i showed a schematic illustration of an LED by using MoS_2 and WSe_2 as the n-type and the p-type material, respectively [171]. In the LED structure, the MoS_2 and WSe_2 were used to inject the electrons and holes, while the sandwiched black phosphorus was used as the trapping site of the injected carriers for light emission.

4.3. Hydrogen Evolution Reaction (HER)

Environmental pollution caused by the consumption of non-renewable fossil energy has made the development of new energy a hot topic in the academic society. Electrocatalytic hydrogen production has been considered as one of the most effective ways to produce clean hydrogen energy. So far, Pt and other noble metals were the best electrocatalysts for a hydrogen evolution reaction. However, limited resources and the high price of noble metals restrict their large-scale application. Thus, the search for new catalysts alternative to Pt is imminent. Among the many-layered TMDs, MoS_2 is the first one to emerge as an active hydrogen evolution reaction catalyst. Bulk MoS_2 was used as a catalyst for HER in the 1970s, but it showed poor catalytic activity (an onset potential of 90 meV and a Tafel slope of 692 mV/dec) [179]. The rapid development of nanotechnology facilitated the exploration of the performance of nanostructured materials. Contrary to bulk MoS_2, MoS_2 nanoparticles were an active HER catalyst, which was demonstrated by Nørskov's group in 2005 [180]. Since then, two-dimensional nanostructured TMDs have attracted extensive research interest as electrocatalysts for hydrogen evolution [181–186].

4.3.1. Increasing the Number of Active Sites

Theoretical calculations and experimental results have revealed that the basal plane of TMDs was catalytically inert, whereas the surface edges were chemically active [56,180,187]. Therefore, increasing the number of active sites is an effective way to enhance their catalytic performance. Liu's group synthesized monolayer MoS_2 on Au foil substrate by using a CVD method [148]. Monolayer triangular shape MoS_2 with different coverage (10%, 20%, 40%, 60%, 80%) was obtained upon varying the growth temperature or the precursor-substrate distance. On increasing the coverage of MoS_2, the average edge length was increased, which was confirmed by representative SEM images. The polarization curves of various samples in Figure 10a indicate that the 80% coverage sample exhibited the lowest onset overpotentials (η) with the value of ~100 mV. At the same time, the 80% coverage sample showed cathodic current density of ~50.5 mA/cm^2 at η = 300 mV, which was much larger than that of 60%, 40%, 20% and 10% samples (15.3, 10.1, 5.7, and 3.9 mA/cm^2, respectively). As shown in Figure 10b, the overall Tafel slopes measured in the range of 61–74 mV/dec and the 80% coverage MoS_2 sample showed the lowest Tafel slope (61 mV/decade). The one-dimensional MoS_2 nanobelts synthesized by our group (details in Section 3.9) had an onset overpotential of −170 mV, lower than that of monolayer MoS_2 (−250 mV) [80]. Compared with monolayer MoS_2 (90 mV/dec), MoS_2 nanobelts showed a smaller Tafel slope (70 mV/dec). The top surface was composed of the edges of the base planes, which provided a high density of edge sites, so that the nanobelts exhibited a more superior catalytic activity than the monolayer MoS_2 (Figure 10c,d).

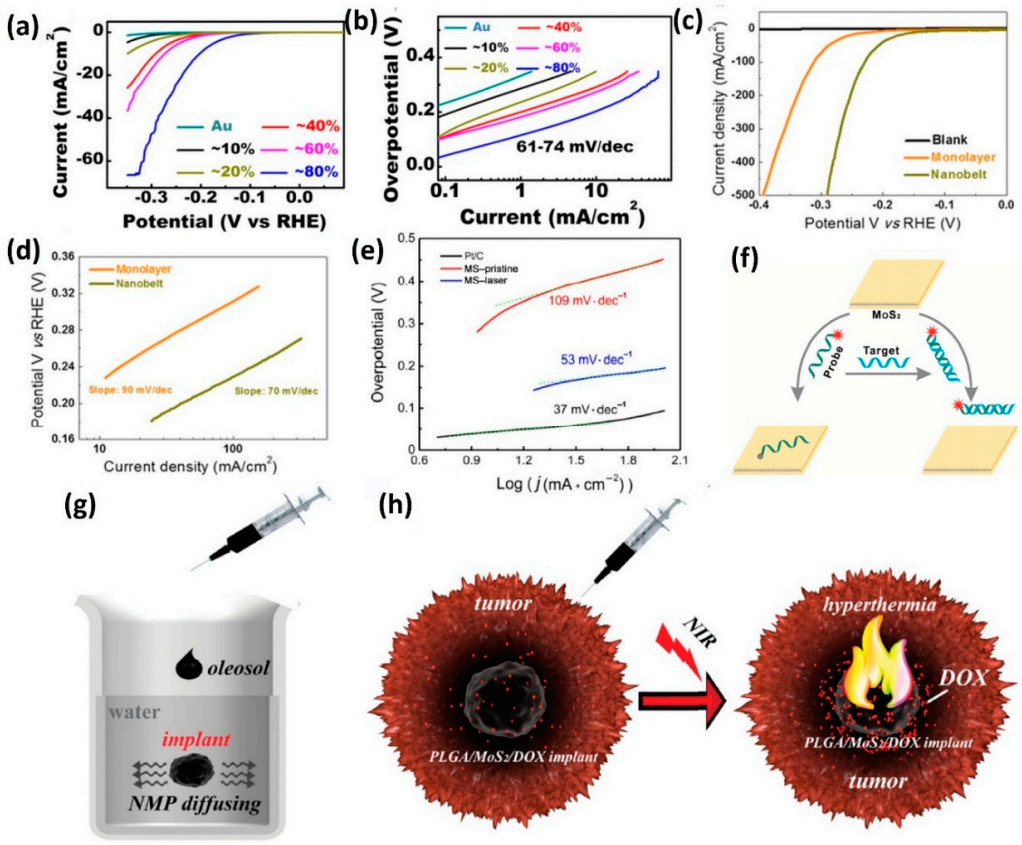

Figure 10. Application of low-dimensional TMDs in HER, hydrogen storage and biosystems. (**a**) Polarization curves of monolayer MoS_2 on Au foils with different coverage. The 80% coverage sample exhibited current density of ~50.5 mA/cm^2 at η = 300 mV, which was much larger than that of the 60%, 40%, 20%, and 10% coverage samples (15.3, 10.1, 5.7and 3.9 mA/cm^2, respectively) [148]. (**b**) Tafel plots of monolayer MoS_2 on Au foils with different coverage. The overall Tafel slopes were in the range of 61–74 mV/decade and the lowest Tafel slope was achieved from the sample with ~80% coverage (61 mV/decade) [148]. (**c**) Polarization curves of monolayer MoS_2 and MoS_2 nanobelts. At the current density of 20 mA/cm^2, the overpotential of monolayer MoS_2 and MoS_2 nanobelts were 170 mV and 250 mV, respectively [80]. (**d**) Tafel plots of monolayer MoS_2 and MoS_2 nanobelts. The Tafel slope of the nanobelts was 70 mV/decade, which was lower than that of monolayer MoS_2 (90 mV/decade) [80]. (**e**) Tafel plots of pristine MoS_2, MoS_2 QDs, and commercial Pt/C. Compared with the pristine MoS_2 (109 mV/dec), the MoS_2 QDs prepared by ultrafast laser ablation showed a much-lower Tafel slope with the value of 53 mV/dec, which was close to the value measured for commercial Pt/C (37 mV/dec) [188]. (**f**) Schematic illustration of the fluorimetric DNA assay. MoS_2 adsorbed dye-labeled single-stranded DNA probe via the van der Waals force between MoS_2 and nucleobases, and then quenched the fluorescence of the probe. Compared with single-stranded DNA probe, the interaction between the formed double-stranded DNA and MoS_2 was weaker, which made the dye-labeled probe away from the surface of MoS_2. As a result, the fluorescence of the probe was recovered [189]. (**g**) PLGA chains in PMD oleosol undergo an immediate liquid–solid phase transformation on contact with water and the MoS_2 nanosheets and anticancer drug DOX encapsulates inside the implant matrix [190]. (**h**) Schematic depiction of the PMD oleosol in tumor therapy with NIR laser irradiation. The MoS_2 showed a high NIR absorbance. With NIR laser irradiation, the generated heat causes significant tumor coagulation necrosis; thus, the tumor can be completely erased without recurrence [190]. Reproduced with permission from [80]. Copyright American Chemical Society, 2015. Reproduced with permission from [148]. Copyright American Chemical Society, 2014. Reproduced with permission from [188]. Copyright Springer, 2017. Reproduced with permission from [189]. Copyright American Chemical Society, 2013. Reproduced with permission from [190]. Copyright Wiley-VCH Verlag GmbH & Co. KGaA, Weinheim, 2015.

TMDs QDs have a higher special surface area and more edge atom, which should benefit the catalytic activity toward HER. Xu et al. studied the electrocatalytic performance of MoS_2 and WS_2 composites (composites of nanosheets and QDs) [191]. The onset overpotential of MoS_2 and WS_2 composites were ~120 mV and ~180 mV, respectively. The MoS_2 and WS_2 composites prepared in DMF and NMP showed the same onset overpotential, which indicated that the solvent had little or no effect on the chemical property and structure of these QDs. For MoS_2 and WS_2 composites, the Tafel slopes ranged from 69 to 75 mV/dec, which were similar to that of MoS_2 nanobelts. The excellent catalytic activity might result from two factors: (1) The QDs might possess unique defect-rich structure that could bring in more active edge sites; (2) the efficiency of electrons transferred between the active edge sites and electrode was enhanced due to the random or disordered stacking of the exfoliated nanosheets on the surface of glass carbon electrode. Recently, Li's group successfully fabricated MoS_2 QDs of about 2 nm diameter by using a facile and general ultrafast laser ablation method [188]. The as-prepared MoS_2 QDs showed significant lattice deformation and high amounts of surface defects. Owing to their large specific surface area, high content of active sites, good hydrophilicity and high conductivity, the MoS_2 QDs exhibited high catalytic activity; the overpotential was 108 mV at 10 mA/cm^{-2}, and the Tafel slope was 53 mV/dec, as shown in Figure 10e.

4.3.2. Optimizing the Electronic Structure

The Gibbs free energy (ΔG_H) for hydrogen adsorption on the active sites plays a key role in the catalytic efficiency of a catalyst; the optimal Gibbs free energy for hydrogen adsorption is close to zero [20,56,180,192,193]. The monolayer $MoS_{2(1-x)}Se_{2x}$ alloys with different Se contents mentioned in Section 3.8 had different electronic structures, confirmed by Raman scattering and PL characterizations [107]. The electrocatalytic activity characterizations indicated that in monolayer MoS_2, the overpotential at the current density of 10 mA/cm^2 was −335 mV, which was larger than that of monolayer $MoS_{2(1-x)}Se_{2x}$ (−300 mV (x = 0.39), −273 mV (x = 0.51) and −279 mV (x = 0.61)). At the same time, the Tafel slope of monolayer $MoS_{2(1-x)}Se_{2x}$ was 100 mV/dec (x = 0.39), 119 mV/dec (x = 0.51), 106 mV/dec (x = 0.61), smaller than that of pure monolayer MoS_2 (134 mV/dec). The Gibbs free energy of hydrogen adsorption is associated with the density of states near the Fermi level. Reduced ΔG_H can be achieved when the density of states near Fermi level is increased. Compared with pure MoS_2, the Mo atoms in $MoS_{2(1-x)}Se_{2x}$ alloys have a lower oxidation state. As a consequence, reduced hydrogen adsorption energy was obtained in $MoS_{2(1-x)}Se_{2x}$ alloys. Therefore, enhanced catalytic performance was achieved in the $MoS_{2(1-x)}Se_{2x}$ alloys compared with pure MoS_2. Similar enhanced catalytic performance was also observed in monolayer $WS_{2(1-x)}Se_{2x}$ alloys [108].

4.3.3. Improving Electrical Conductivity

Increasing electrical transport is another efficient way to increase electrocatalytic performance because high conductivity can effectively facilitate electron transport during the catalytic process. Lukowski and co-workers transformed the MoS_2 from the semiconductor phase to the metal phase via lithium intercalation [194]. The formation of the 1T-MoS_2 after lithium intercalation was confirmed by X-ray diffraction, Raman scattering, HRTEM, etc. In an acidic electrolyte, the 2H-MoS_2 had onset overpotential (at a current density of 10 mA/cm^2) of −320 mV, and Tafel slope of 110 mV/dec. However in 1T-MoS_2, as expected, it exhibited enhanced HER activities—onset overpotential was −195 mV vs. RHE, and Tafel slope was 43 mV/dec, respectively. Besides phase transformation, growing low-dimensional TMDs on conductive substrates or fabricating TMDs-based heterostructures can also be used to improve their electrical conductivity [195–198]. As discussed in Section 3.8, $WS_{2(1-x)}Se_{2x}$ nanotubes were successfully synthesized on conductive CFs [45]. When the $WS_{2(1-x)}Se_{2x}$ nanotubes on CFs served as working electrodes for HER, they exhibited excellent electrocatalytic performance.

4.4. Electrochemical Hydrogen Storage

Besides hydrogen production, hydrogen storage is also a challenge in hydrogen technology. As mentioned in Section 3.9, one-dimensional MoS_2 nanotube could be synthesized by directly heating $(NH_4)_2MoS_4$ in hydrogen/thiophene atmosphere [158]. Chen et al. examined the electrochemical hydrogen storage property by measuring the cyclic voltamogram, in which the reduction and oxidation process corresponded to the hydrogen adsorption and desorption, respectively. The hydrogen adsorption amount on MoS_2 nanotubes obtained by the electrochemical method showed the highest, comparing to previous reported work, and the highest capacity was 260 mAh/g (corresponding to the formula of $H_{1.57}MoS_2$, 0.97 wt.% hydrogen) at 50 mA/g and 20 °C. The high capacity of the MoS_2 nanotube was attributed to the enhanced electrochemical catalytic activity of its highly nanoporous structure. Meanwhile, they believed that the physicochemical interaction was responsible for the high hydrogen adsorption of MoS_2 nanotubes. However, further research work is still necessary to understand the precise nature of the interaction between hydrogen and MoS_2 nanotubes during storage.

4.5. Biosystems

Biomolecular detection plays a key role in the fields of medical diagnostics, drug discovery, food safety, environmental monitoring, and so on. Zhang's group reported the detection of DNA and small molecules by using MoS_2 nanosheets as a sensing platform [189]. Their ideas were from findings that the Mo ions in MoS_2 possessed intrinsic fluorescence-quenching properties and MoS_2 showed different affinities toward single-stranded DNA versus double-stranded DNA. MoS_2 adsorbed dye-labeled single-stranded DNA probe via the van der Waals force between MoS_2 and nucleobases, and then quenched the fluorescence of the probe. When a single-stranded DNA probe was hybridized with its complementary target DNA, the double-stranded DNA was formed. Compared to single-stranded DNA probe, interaction between the formed double-stranded DNA and MoS_2 was weaker, which led the dye-labeled probe away from the surface of MoS_2. As a result, the fluorescence of the probe was recovered and was used to read the quantity of the target DNA. Figure 10f schematically describes the whole process.

The TMDs can accommodate a large mass of drugs, which offers great potential in pharmaceutical applications [96]. For example, they could act as drug carriers and deliver the drugs to the specified cells. As drug carriers, drug-loading capability is a very important parameter [96]. For 2D TMDs, the highest-reported drug loading ratio (weight ratios between the drug and 2D TMDs) were determined as ≈240%, higher than that of graphene oxide (≈150%). Moreover, 2D TMDs also show a high near infra-red (NIR) absorbance, which make them suitable for photo thermal ablation of diseases such as tumors [98]. For localized tumor-synergistic therapy, Wang et al. prepared the phase-changing organic-inorganic PLGA/MoS_2/DOX composite oleosol by homogenizing PLGA, MoS_2 and DOX together into the NMP solvent, where the PLGA referred to Poly (lactic- co -glycolic acid), and the DOX referred to doxorubicin [190]. When the PLGA/MoS_2/DOX oleosol came in contact with body fluid, unlike the traditional drug/carrier manner of "dispersed-in-suspension", the oleosol would immediately solidify (Figure 10g), and the MoS_2 nanosheets and anticancer drug DOX was encapsulated inside the implant matrix. Therefore, a solid implant with high potential in synergistic tumor photo thermal and chemotherapy was formed. With NIR laser irradiation, the generated heat causes significant tumor coagulation necrosis; thus, the tumor can be completely erased without recurrence. The schematic process is shown in Figure 10h.

TMDs QDs could also be used in cancer radiation therapies [139]. Experimental investigations indicate that the cysteine-protected WS_2 QDs exhibit strong catalytic activities toward the reduction of H_2O_2 and O_2, and showed excitation-wavelength dependent fluorescence. These properties made the WS_2 QDs a potential candidate to improve cell viabilities and eliminate reactive oxygen species in injured cells. In vivo studies showed that the WS_2 QDs could also prevent DNA damages in irradiated cells under exposure to high-energy gamma rays. At the same time, the cysteine-protected WS_2 QDs could recover superoxide dismutase and remove excessive Methylenedioxyamphetamine in the liver

and lung by participating in the catalytic processes and omitting reactive oxygen species. Furthermore, nearly 80% of WS_2 QDs was rapidly excreted through renal routes 1 day post injection and no notable toxicological responses was found up to 30 days at a relatively high injection dose.

5. Summary and Outlook

This review has summarized recent developments in the preparation of low-dimensional TMDs. Several methods such as mechanical cleavage method, liquid exfoliation method, Li-intercalation exfoliation method, laser and plasma-induced thinning method, CVD method and so on have been adopted to prepare low-dimensional TMDs. In view of their fascinating properties and diverse preparation methods, low-dimensional TMDs have been utilized in many ways, such as devices, energy, biosystems, etc. Although significant achievements have been made in low-dimensional TMDs related areas, there were several problems. Taking MoS_2 as an example, the room-temperature top and back gated configuration field-effect mobility were ~200 $cm^2 \cdot V^{-1} \cdot s^{-1}$ and ~1.2 $cm^2 \cdot V^{-1} \cdot s^{-1}$, respectively, which was much lower than that of silicon (~1400 $cm^2 \cdot V^{-1} \cdot s^{-1}$). To replace silicon in semiconductor chips, further improvement of the electrical performance of TMDs-based devices is necessary. TMDs-based catalysts have exhibited excellent electrocatalytic performance, although their HER activities were still inferior to noble metals like Pt. Thus, further enhancement of the electrocatalytic performance of TMDs is essential and imperative. Mass production of high-quality TMDs remains challenging because the size of a single crystal of TMDs obtained from the methods mentioned above is about dozens of microns, which is insufficient for industrial applications. As discussed in Section 4.3, the EQE of TMDs based diodes was still very low, compared to materials used in the industry. Ways to increase EQE should concentrated on improving the quality of materials and optimizing the interface, because the physical transfer and sequential chemical synthesis of the initial layers can damage the intrinsic structure and influence the physical properties of the layers.

Theoretical calculations and experimental results indicate that the plane edges of semiconductor TMDs are metallic, but the electronic transport properties and their application in devices is still unknown. To gain a better understanding of the electronic transport performance of TMDs, it is worth specializing in the synthesis of TMDs with totally exposed metallic edges and fabrication of metallic edges-based FET. Meanwhile, it is meaningful to fabricate hetero-dimensional nanostructures with TMDs nanowires metallic edges that have been contacted with monolayer TMDs, forming FET with metallic edge electrodes. Studies on contact resistance between the source/drain electrodes and the channel and the performance of the FET are also a possibility.

Diluted magnetic semiconductors (DMSs) have attracted great interest because they combine two large branches in one material—the charge degree of freedom of electrons in semiconductors and the spin degree of freedom in magnetic materials. The coexistence of ferromagnetism and semiconducting properties can be realized by introducing magnetic elements into nonmagnetic semiconductors. At present, studies on DMSs are centered mostly on III-V and II-VI based DMSs, such as (Cd, Mn)Te, (Zn, Mn)S, (In, Mn)As and (Ga, Mn)As. However, TMDs-based DMSs have never been involved. The successful synthesis of few-layer TMDs alloying with magnetic elements will enrich the DMSs family and trigger fascinating properties due to their special structure.

Author Contributions: L.Y., R.N.A., C.F. and B.X. contributed to the conception and the writing of this paper. C.X., J.J. and P.L. contributed to the revision of this paper.

Funding: This research was funded by the Scientific Research Foundation for High-Level Talents of West Anhui University (WGKQ201702004), the Youth Program of West Anhui University (WXZR201807) and the joint fund of the National Natural Science Foundation Committee of China Academy of Engineering Physics (NSAF) (U1630108).

Acknowledgments: This work was supported by the Scientific Research Foundation for High-Level Talents of West Anhui University (WGKQ201702004), the Youth Program of West Anhui University (WXZR201807) and the joint fund of the National Natural Science Foundation Committee of China Academy of Engineering Physics (NSAF) (U1630108). This work was partially carried out at the USTC Center for Micro and Nanoscale Research and Fabrication.

Conflicts of Interest: The authors declare no conflicts of interest.

References

1. Novoselov, K.S.; Geim, A.K.; Morozov, S.V.; Jiang, D.; Zhang, Y.; Dubonos, S.V.; Grigorieva, I.V.; Firsov, A.A. Electric field effect in atomically thin carbon films. *Science* **2004**, *306*, 666–669. [CrossRef] [PubMed]
2. Butler, S.Z.; Hollen, S.M.; Cao, L.; Cui, Y.; Gupta, J.A.; Gutiérrez, H.R.; Heinz, T.F.; Hong, S.S.; Huang, J.; Ismach, A.F.; et al. Progress, challenges, and opportunities in two-dimensional materials beyond graphene. *ACS Nano* **2013**, *7*, 2898–2926. [CrossRef] [PubMed]
3. Xu, M.; Liang, T.; Shi, M.; Chen, H. Graphene-like two-dimensional materials. *Chem. Rev.* **2013**, *113*, 3766–3798. [CrossRef] [PubMed]
4. de Castro, I.A.; Datta, R.S.; Ou, J.Z.; Castellanos-Gomez, A.; Sriram, S.; Daeneke, T.; Kalantar-zadeh, K. Molybdenum oxides—From fundamentals to functionality. *Adv. Mater.* **2017**, *29*, 1701619. [CrossRef] [PubMed]
5. Vaughn, D.D., II; Schaak, R.E. Synthesis, properties and applications of colloidal germanium and germanium-based nanomaterials. *Chem. Soc. Rev.* **2013**, *42*, 2861–2879. [CrossRef] [PubMed]
6. Liu, H.; Du, Y.; Deng, Y.; Ye, P.D. Semiconducting black phosphorus: Synthesis, transport properties and electronic applications. *Chem. Soc. Rev.* **2015**, *44*, 2732–2743. [CrossRef] [PubMed]
7. Jiang, X.-D.; Weng, Q.; Wang, X.-B.; Li, X.; Zhang, J.; Golberg, D.; Bando, Y. Recent progress on fabrications and applications of boron nitride nanomaterials: A review. *J. Mater. Sci. Technol.* **2015**, *31*, 589–598. [CrossRef]
8. Ginley, T.P.; Wang, Y.; Law, S. Topological insulator film growth by molecular beam epitaxy: A review. *Crystals* **2016**, *6*, 154. [CrossRef]
9. Koppens, F.H.L.; Mueller, T.; Avouris, P.; Ferrari, A.C.; Vitiello, M.S.; Polini, M. Photodetectors based on graphene, other two-dimensional materials and hybrid systems. *Nat. Nanotechnol.* **2014**, *9*, 780–793. [CrossRef] [PubMed]
10. Fiori, G.; Bonaccorso, F.; Iannaccone, G.; Palacios, T.; Neumaier, D.; Seabaugh, A.; Banerjee, S.K.; Colombo, L. Electronics based on two-dimensional materials. *Nat. Nanotechnol.* **2014**, *9*, 768–779. [CrossRef] [PubMed]
11. Fu, Q.; Bao, X. Surface chemistry and catalysis confined under two-dimensional materials. *Chem. Soc. Rev.* **2017**, *46*, 1842–1874. [CrossRef] [PubMed]
12. Kuc, A.; Zibouche, N.; Heine, T. Influence of quantum confinement on the electronic structure of the transition metal sulfide TS_2. *Phys. Rev. B* **2011**, *83*, 245213. [CrossRef]
13. Ding, Y.; Wang, Y.; Ni, J.; Shi, L.; Shi, S.; Tang, W. First principles study of structural, vibrational and electronic properties of graphene-like MX_2 (M = Mo, Nb, W, Ta; X = S, Se, Te) monolayers. *Phys. B Condens. Matter* **2011**, *406*, 2254–2260. [CrossRef]
14. Liu, L.; Kumar, S.B.; Ouyang, Y.; Guo, J. Performance limits of monolayer transition metal dichalcogenide transistors. *IEEE Trans. Electron. Devices* **2011**, *58*, 3042–3047. [CrossRef]
15. Yu, Y.; Yang, F.; Lu, X.F.; Yan, Y.J.; Cho, Y.-H.; Ma, L.; Niu, X.; Kim, S.; Son, Y.-W.; Feng, D.; et al. Gate-tunable phase transitions in thin flakes of 1T-TaS_2. *Nat. Nanotechnol.* **2015**, *10*, 270–276. [CrossRef] [PubMed]
16. Zhang, Y.; Ye, J.; Matsuhashi, Y.; Iwasa, Y. Ambipolar MoS_2 thin flake transistors. *Nano Lett.* **2012**, *12*, 1136–1140. [CrossRef] [PubMed]
17. Gao, Y.; Liu, Z.; Sun, D.-M.; Huang, L.; Ma, L.-P.; Yin, L.-C.; Ma, T.; Zhang, Z.; Ma, X.-L.; Peng, L.-M.; et al. Large-area synthesis of high-quality and uniform monolayer WS_2 on reusable Au foils. *Nat. Commum.* **2015**, *6*, 8569. [CrossRef] [PubMed]
18. Chhowalla, M.; Shin, H.S.; Eda, G.; Li, L.-J.; Loh, K.P.; Zhang, H. The chemistry of two-dimensional layered transition metal dichalcogenide nanosheets. *Nat. Chem.* **2013**, *5*, 263–275. [CrossRef] [PubMed]
19. Lv, R.; Robinson, J.A.; Schaak, R.E.; Sun, D.; Sun, Y.; Mallouk, T.E.; Terrones, M. Transition metal dichalcogenides and beyond: Synthesis, properties, and applications of single- and few-layer nanosheets. *Acc. Chem. Res.* **2015**, *48*, 56–64. [CrossRef] [PubMed]
20. Kam, K.K.; Parklnclon, B.A. Detailed photocurrent spectroscopy of the semiconducting group transition metal dichalcogenides. *J. Phys. Chem.* **1982**, *86*, 463–467. [CrossRef]
21. Mak, K.F.; Lee, C.; Hone, J.; Shan, J.; Heinz, T.F. Atomically thin MoS_2: A new direct-gap semiconductor. *Phys. Rev. Lett.* **2010**, *105*, 136805. [CrossRef] [PubMed]

22. Li, H.; Wu, J.; Yin, Z.; Zhang, H. Preparation and applications of mechanically exfoliated single-layer and multilayer MoS_2 and WSe_2 nanosheets. *Acc. Chem. Res.* **2014**, *47*, 1067–1075. [CrossRef] [PubMed]
23. Mak, K.F.; He, K.; Lee, C.; Lee, G.H.; Hone, J.; Heinz, T.F.; Shan, J. Tightly bound trions in monolayer MoS_2. *Nat. Mater.* **2013**, *12*, 207–211. [CrossRef] [PubMed]
24. Xiao, D.; Liu, G.-B.; Feng, W.; Xu, X.; Yao, W. Coupled spin and valley physics in monolayers of MoS_2 and other group-VI dichalcogenides. *Phys. Rev. Lett.* **2012**, *108*, 196802. [CrossRef] [PubMed]
25. Eknapakul, T.; King, P.D.C.; Asakawa, M.; Buaphet, P.; He, R.-H.; Mo, S.-K.; Takagi, H.; Shen, K.M.; Baumberger, F.; Sasagawa, T.; et al. Electronic structure of a quasi-freestanding MoS_2 monolayer. *Nano Lett.* **2014**, *14*, 1312–1316. [CrossRef] [PubMed]
26. Zhao, Y.; Luo, X.; Li, H.; Zhang, J.; Araujo, P.T.; Gan, C.K.; Wu, J.; Zhang, H.; Quek, S.Y.; Dresselhaus, M.S.; et al. Interlayer breathing and shear modes in few-trilayer MoS_2 and WSe_2. *Nano Lett.* **2013**, *13*, 1007–1015. [CrossRef] [PubMed]
27. Li, Y.; Zhou, Z.; Zhang, S.; Chen, Z. MoS_2 nanoribbons: High stability and unusual electronic and magnetic properties. *J. Am. Chem. Soc.* **2008**, *130*, 16739–16744. [CrossRef] [PubMed]
28. Cai, Y.; Zhang, G.; Zhang, Y.W. Polarity-reversed robust carrier mobility in monolayer MoS_2 nanoribbons. *J. Am. Chem. Soc.* **2014**, *136*, 6269–6275. [CrossRef] [PubMed]
29. Gan, Z.X.; Liu, L.Z.; Wu, H.Y.; Hao, Y.L.; Shan, Y.; Wu, X.L.; Chu, P.K. Quantum confinement effects across two-dimensional planes in MoS_2 quantum dots. *Appl. Phys. Lett.* **2015**, *106*, 233113. [CrossRef]
30. Novoselov, K.S.; Jiang, D.; Schedin, F.; Booth, T.J.; Khotkevich, V.V.; Morozov, S.V.; Geim, A.K. Two-dimensional atomic crystals. *Proc. Natl. Acad. Sci. USA* **2005**, *102*, 10451–10453. [CrossRef] [PubMed]
31. Radisavljevic, B.; Radenovic, A.; Brivio, J.; Giacometti, V.; Kis, A. Single-layer MoS_2 transistors. *Nat. Nanotechnol.* **2011**, *6*, 147–150. [CrossRef] [PubMed]
32. Coleman, J.N.; Lotya, M.; O'Neill, A.; Bergin, S.D.; King, P.J.; Khan, U.; Young, K.; Gaucher, A.; De, S.; Smith, R.J.; et al. Two-dimensional nanosheets produced by liquid exfoliation of layered materials. *Science* **2011**, *331*, 568–571. [CrossRef] [PubMed]
33. Zhou, K.-G.; Mao, N.-N.; Wang, H.-X.; Peng, Y.; Zhang, H.-L. A mixed-solvent strategy for efficient exfoliation of inorganic graphene analogues. *Angew. Chem. Int. Ed.* **2011**, *50*, 10839–10842. [CrossRef] [PubMed]
34. Smith, R.J.; King, P.J.; Lotya, M.; Wirtz, C.; Khan, U.; De, S.; O'Neill, A.; Duesberg, G.S.; Grunlan, J.C.; Moriarty, G.; et al. Large-scale exfoliation of inorganic layered compounds in aqueous surfactant solutions. *Adv. Mater.* **2011**, *23*, 3944–3948. [CrossRef] [PubMed]
35. Joensen, P.; Frindt, R.F.; Morrison, S.Y. Single-layer MoS_2. *Mater. Res. Bull.* **1986**, *21*, 457–461. [CrossRef]
36. Zeng, Z.; Yin, Z.; Huang, X.; Li, H.; He, Q.; Lu, G.; Boey, F.; Zhang, H. Single-layer semiconducting nanosheets: High-yield preparation and device fabrication. *Angew. Chem. Int. Ed.* **2011**, *50*, 11093–11097. [CrossRef] [PubMed]
37. Castellanos-Gomez, A.; Barkelid, M.; Goossens, A.M.; Calado, V.E.; van der Zant, H.S.J.; Steele, G.A. Laser-thinning of MoS_2: On demand generation of a single-layer semiconductor. *Nano Lett.* **2012**, *12*, 3187–3192. [CrossRef] [PubMed]
38. Liu, Y.; Nan, H.; Wu, X.; Pan, W.; Wang, W.; Bai, J.; Zhao, W.; Sun, L.; Wang, X.; Ni, Z. Layer-by-layer thinning of MoS_2 by plasma. *ACS Nano* **2013**, *7*, 4202–4209. [CrossRef] [PubMed]
39. Yang, L.; Cui, X.; Zhang, J.; Wang, K.; Shen, M.; Zeng, S.; Dayeh, S.A.; Feng, L.; Xiang, B. Lattice strain effects on the optical properties of MoS_2 nanosheets. *Sci. Rep.* **2014**, *4*, 5649. [CrossRef] [PubMed]
40. Zhu, X.; Xiang, J.; Li, J.; Feng, C.; Liu, P.; Xiang, B. Tunable photoluminescence of MoS_2 quantum dots passivated by different functional groups. *J. Colloid Interface Sci.* **2018**, *511*, 209–214. [CrossRef] [PubMed]
41. Lee, Y.-H.; Zhang, X.-Q.; Zhang, W.; Chang, M.-T.; Lin, C.-T.; Chang, K.-D.; Yu, Y.-C.; Wang, J.T.-W.; Chang, C.-S.; Li, L.-J.; et al. Synthesis of large-area MoS_2 atomic layers with chemical vapor deposition. *Adv. Mater.* **2012**, *24*, 2320–2325. [CrossRef] [PubMed]
42. Lee, Y.-H.; Yu, L.; Wang, H.; Fang, W.; Ling, X.; Shi, Y.; Lin, C.-T.; Huang, J.-K.; Chang, M.-T.; Chang, C.-S.; et al. Synthesis and transfer of single-layer transition metal disulfides on diverse surfaces. *Nano Lett.* **2013**, *13*, 1852–1857. [CrossRef] [PubMed]
43. Huang, J.; Yang, L.; Liu, D.; Chen, J.; Fu, Q.; Xiong, Y.; Lin, F.; Xiang, B. Large-area synthesis of monolayer WSe_2 on a SiO_2/Si substrate and its device applications. *Nanoscale* **2015**, *7*, 4193–4198. [CrossRef] [PubMed]
44. Zhang, W.; Huang, J.-K.; Chen, C.-H.; Chang, Y.-H.; Cheng, Y.-J.; Li, L.-J. High-gain phototransistors based on a CVD MoS_2 monolayer. *Adv. Mater.* **2013**, *25*, 3456–3461. [CrossRef] [PubMed]

45. Xu, K.; Wang, F.; Wang, Z.; Zhan, X.; Wang, Q.; Cheng, Z.; Safdar, M.; He, J. Component-controllable $WS_{2(1-x)}Se_{2x}$ nanotubes for efficient hydrogen evolution reaction. *ACS Nano* **2014**, *8*, 8468–8476. [CrossRef] [PubMed]
46. van der Zande, A.M.; Huang, P.Y.; Chenet, D.A.; Berkelbach, T.C.; You, Y.; Lee, G.-H.; Heinz, T.F.; Reichman, D.R.; Muller, D.A.; Hone, J.C. Grains and grain boundaries in highly crystalline monolayer molybdenum disulphide. *Nat. Mater.* **2013**, *12*, 554–561. [CrossRef] [PubMed]
47. Lin, Y.-C.; Zhang, W.; Huang, J.-K.; Liu, K.-K.; Lee, Y.-H.; Liang, C.-T.; Chud, C.-W.; Li, L.-J. Wafer-scale MoS_2 thin layers prepared by MoO_3 sulfurization. *Nanoscale* **2012**, *4*, 6637–6641. [CrossRef] [PubMed]
48. Feng, Q.; Zhu, Y.; Hong, J.; Zhang, M.; Duan, W.; Mao, N.; Wu, J.; Xu, H.; Dong, F.; Lin, F.; et al. Growth of large-area 2D $MoS_{2(1-x)}$ Se_{2x} semiconductor alloys. *Adv. Mater.* **2014**, *26*, 2648–2653. [CrossRef] [PubMed]
49. Xu, G.; Wang, X.; Sun, Y.; Chen, X.; Zheng, J.; Sun, L.; Jiao, L.; Li, J. Metallic and ferromagnetic MoS_2 nanobelts with vertically aligned edges. *Nano Res.* **2015**, *8*, 2946–2953. [CrossRef]
50. Li, S.; Lin, Y.-C.; Zhao, W.; Wu, J.; Wang, Z.; Hu, Z.; Shen, Y.; Tang, D.-M.; Wang, J.; Zhang, Q.; et al. Vapour–liquid–solid growth of monolayer MoS_2 nanoribbons. *Nat. Mater.* **2018**, *17*, 535–542. [CrossRef] [PubMed]
51. Liu, K.-K.; Zhang, W.; Lee, Y.-H.; Lin, Y.-C.; Chang, M.-T.; Su, C.-Y.; Chang, C.-S.; Li, H.; Shi, Y.; Zhang, H.; et al. Growth of large-area and highly crystalline MoS_2 thin layers on insulating substrates. *Nano Lett.* **2012**, *12*, 1538–1544. [CrossRef] [PubMed]
52. Nath, M.; Govindaraj, A.; Rao, C.N.R. Simple synthesis of MoS_2 and WS_2 nanotubes. *Adv. Mater.* **2001**, *13*, 283–286. [CrossRef]
53. Hu, D.; Xu, G.; Xing, L.; Yan, X.; Wang, J.; Zheng, J.; Lu, Z.; Wang, P.; Pan, X.; Jiao, L. Two-dimensional semiconductors grown by chemical vapor transport. *Angew. Chem. Int. Ed.* **2017**, *56*, 3611–3615. [CrossRef] [PubMed]
54. Fathipour, S.; Remskar, M.; Varlec, A.; Ajoy, A.; Yan, R.; Vishwanath, S.; Rouvimov, S.; Hwang, W.S.; Xing, H.G.; Jena, D.; et al. Synthesized multiwall MoS_2 nanotube and nanoribbon field-effect transistors. *Appl. Phys. Lett.* **2015**, *106*, 022114. [CrossRef]
55. Kibsgaard, J.; Chen, Z.; Reinecke, B.N.; Jaramillo, T.F. Engineering the surface structure of MoS_2 to preferentially expose active edge sites for electrocatalysis. *Nat. Mater.* **2012**, *11*, 963–969. [CrossRef] [PubMed]
56. Voiry, D.; Yamaguchi, H.; Li, J.; Silva, R.; Alves, D.C.B.; Fujita, T.; Chen, M.; Asefa, T.; Shenoy, V.B.; Eda, G.; et al. Enhanced catalytic activity in strained chemically exfoliated WS_2 nanosheets for hydrogen evolution. *Nat. Mater.* **2013**, *12*, 850–855. [CrossRef] [PubMed]
57. Yan, Y.; Xia, B.Y.; Xu, Z.; Wang, X. Recent development of molybdenum sulfides as advanced electrocatalysts for hydrogen evolution reaction. *ACS Catal.* **2014**, *4*, 1693–1705. [CrossRef]
58. Xu, C.; Peng, S.; Tan, C.; Ang, H.; Tan, H.; Zhang, H.; Yan, Q. Ultrathin S-doped $MoSe_2$ nanosheets for efficient hydrogen evolution. *J. Mater. Chem. A* **2014**, *2*, 5597–5601. [CrossRef]
59. Manzeli, S.; Ovchinnikov, D.; Pasquier, D.; Yazyev, O.V.; Kis, A. 2D transition metal dichalcogenides. *Nat. Rev. Mater.* **2017**, *2*, 17033. [CrossRef]
60. Li, H.; Li, Y.; Aljarb, A.; Shi, Y.; Li, L.-J. Epitaxial growth of two-dimensional layered transition-metal dichalcogenides: Growth mechanism, controllability, and scalability. *Chem. Rev.* **2017**. [CrossRef] [PubMed]
61. Li, S.-L.; Tsukagoshi, K.; Orgiu, E.; Samorı, P. Charge transport and mobility engineering in two-dimensional transition metal chalcogenide semiconductors. *Chem. Soc. Rev.* **2016**, *45*, 118–151. [CrossRef] [PubMed]
62. Gao, Y.P.; Wu, X.; Huang, K.-J.; Xing, L.-L.; Zhang, Y.-Y.; Liu, L. Two-dimensional transition metal diseleniums for energy storage application: A review of recent developments. *CrystEngComm* **2017**, *19*, 404–418. [CrossRef]
63. Hu, Z.; Wu, Z.; Han, C.; He, J.; Ni, Z.; Chen, W. Two-dimensional transition metal dichalcogenides: Interface and defect engineering. *Chem. Soc. Rev.* **2018**, *47*, 3100–3128. [CrossRef] [PubMed]
64. Thanh, T.D.; Chuong, N.D.; Hien, H.V.; Kshetri, T.; Tuan, L.H.; Kim, N.H.; Lee, J.H. Recent advances in two-dimensional transition metal dichalcogenides-graphene heterostructured materials for electrochemical applications. *Prog. Mater. Sci.* **2018**, *96*, 51–85. [CrossRef]
65. Wang, Y.-H.; Huang, K.-J.; Wu, X. Recent advances in transition-metal dichalcogenides based electrochemical biosensors: A review. *Biosens. Bioelectron.* **2017**, *97*, 305–316. [CrossRef] [PubMed]

66. Yuan, H.; Kong, L.; Li, T.; Zhang, Q. A review of transition metal chalcogenide/graphene nanocomposites for energy storage and conversion. *Chin. Chem. Lett.* **2017**, *28*, 2180–2194. [CrossRef]
67. Choi, W.; Choudhary, N.; Han, G.H.; Park, J.; Akinwande, D.; Lee, Y.H. Recent development of two-dimensional transition metal dichalcogenides and their applications. *Mater. Today* **2017**, *20*, 116–130. [CrossRef]
68. Duan, X.; Xu, J.; Wei, Z.; Ma, J.; Guo, S.; Liu, H.; Dou, S. Atomically thin transition-metal dichalcogenides for electrocatalysis and energy storage. *Small Methods* **2017**, *1*, 1700156. [CrossRef]
69. Xia, C.; Li, J. Recent advances in optoelectronic properties and applications of two-dimensional metal chalcogenides. *J. Semicond.* **2016**, *37*, 051001. [CrossRef]
70. Wang, Q.H.; Kalantar-Zadeh, K.; Kis, A.; Coleman, J.N.; Strano, M.S. Electronics and optoelectronics of two-dimensional transition metal dichalcogenides. *Nat. Nanotechnol.* **2012**, *7*, 699–712. [CrossRef] [PubMed]
71. Duerloo, K.-A.N.; Li, Y.; Reed, E.J. Structural phase transitions in two-dimensional Mo- and W-dichalcogenide monolayers. *Nat. Commum.* **2014**, *5*, 4214. [CrossRef] [PubMed]
72. Eda, G.; Yamaguchi, H.; Voiry, D.; Fujita, T.; Chen, M.; Chhowalla, M. Photoluminescence from chemically exfoliated MoS_2. *Nano Lett.* **2011**, *11*, 5111–5116. [CrossRef] [PubMed]
73. Lin, Y.C.; Dumcenco, D.O.; Huang, Y.S.; Suenaga, K. Atomic mechanism of the semiconducting-to-metallic phase transition in single-layered MoS_2. *Nat. Nanotechnol.* **2014**, *9*, 391–396. [CrossRef] [PubMed]
74. Wang, L.; Xu, Z.; Wang, W.; Bai, X. Atomic mechanism of dynamic electrochemical lithiation processes of MoS_2 nanosheets. *J. Am. Chem. Soc.* **2014**, *136*, 6693–6697. [CrossRef] [PubMed]
75. Yu, Y.; Nam, G.-H.; He, Q.; Wu, X.-J.; Zhang, K.; Yang, Z.; Chen, J.; Ma, Q.; Zhao, M.; Liu, Z.; et al. High phase-purity 1T′-MoS_2-and 1T′-$MoSe_2$-layered crystals. *Nat. Chem.* **2018**, *10*, 638–643. [CrossRef] [PubMed]
76. Huang, X.; Zeng, Z.; Zhang, H. Metal dichalcogenide nanosheets: Preparation, properties and applications. *Chem. Soc. Rev.* **2013**, *42*, 1934–1946. [CrossRef] [PubMed]
77. Wilson, J.A.; Yoffe, A.D. The transition metal dichalcogenides discussion and interpretation of the observed optical, electrical and structural properties. *Adv. Phys.* **1969**, *18*, 193–335. [CrossRef]
78. Li, J.; Cheng, S.; Liu, Z.; Zhang, W.; Chang, H. Centimeter-scale, large-area, few-layer 1T′-WTe_2 films by chemical vapor deposition and its long-term stability in ambient condition. *J. Phys. Chem. C* **2018**, *122*, 7005–7012. [CrossRef]
79. Manoj, K.J.; Anjali, S.; Dattatray, J.L.; Catherine, R.R.; Kanishka, B.; Claudia, F.; Umesh, V.W.; Rao, C.N.R.A. Combined experimental and theoretical study of the structural, electronic and vibrational properties of bulk and few-layer Td-WTe_2. *J. Phys. Condens. Matter* **2015**, *27*, 285401.
80. Yang, L.; Hong, H.; Fu, Q.; Huang, Y.; Zhang, J.; Cui, X.; Fan, Z.; Liu, K.; Xiang, B. Single-crystal atomic-layered molybdenum disulfide nanobelts with high surface activity. *ACS Nano* **2015**, *9*, 6478–6483. [CrossRef] [PubMed]
81. Seifert, G.; Terrones, H.; Terrones, M.; Jungnickel, G.; Frauenheim, T. Structure and electronic properties of MoS_2 nanotubes. *Phys. Rev. Lett.* **2000**, *85*, 146–149. [CrossRef] [PubMed]
82. Helveg, S.; Lauritsen, J.V.; Lægsgaard, E.; Stensgaard, I.; Nørskov, J.K.; Clausen, B.S.; Topsøe, H.; Besenbacher, F. Atomic-scale structure of single-layer MoS_2 nanoclusters. *Phys. Rev. Lett.* **2000**, *84*, 951–954. [CrossRef] [PubMed]
83. Hansen, L.P.; Ramasse, Q.M.; Kisielowski, C.; Brorson, M.; Johnson, E.; Topsøe, H.; Helveg, S. Atomic-scale edge structures on industrial-style MoS_2 nanocatalysts. *Angew. Chem. Int. Ed.* **2011**, *50*, 10153–10156. [CrossRef] [PubMed]
84. Kisielowski, C.; Ramasse, Q.M.; Hansen, L.P.; Brorson, M.; Carlsson, A.; Molenbroek, A.M.; Topsøe, H.; Helveg, S. Imaging MoS_2 nanocatalysts with single-atom sensitivity. *Angew. Chem. Int. Ed.* **2010**, *122*, 2768–2770. [CrossRef]
85. Lauritsen, J.V.; Kibsgaard, J.; Helveg, S.; Topsøe, H.; Clausen, B.S.; Lægsgaard, E.; Besenbacher, F. Size-dependent structure of MoS_2 nanocrystals. *Nat. Nanotechnol.* **2007**, *2*, 53–58. [CrossRef] [PubMed]
86. Najmaei, S.; Liu, Z.; Zhou, W.; Zou, X.; Shi, G.; Lei, S.; Yakobson, B.I.; Idrobo, J.C.; Ajayan, P.M.; Lou, J. Vapour phase growth and grain boundary structure of molybdenum disulphide atomic layers. *Nat. Mater.* **2013**, *12*, 754–759. [CrossRef] [PubMed]
87. Gong, Y.; Liu, Z.; Lupini, A.R.; Shi, G.; Lin, J.; Najmaei, S.; Lin, Z.; Elías, A.L.; Berkdemir, A.; You, G.; et al. Band gap engineering and layer-by-layer mapping of selenium-doped molybdenum disulfide. *Nano Lett.* **2014**, *14*, 442–449. [CrossRef] [PubMed]

88. Pennycook, S.J. *Progress in Transmission Electron Microscopy*, 1st ed.; Tsinghua University Press: Beijing, China, 1999; Volume 1, p. 97. ISBN 978-35-4067-681-2.
89. Zhang, L.; Wan, L.; Yu, Y.; Wang, B.; Xu, F.; Wei, Y.; Zhao, Y. Modulation of electronic structure of armchair MoS_2 nanoribbon. *J. Phys. Chem. C* **2015**, *119*, 22164–22171. [CrossRef]
90. Wang, R.; Zhou, X.; Xu, X.; Hu, J.; Pan, J. The indirect–direct band gap tuning in armchair MoS_2 nanoribbon by edge passivation. *J. Phys. D Appl. Phys.* **2017**, *50*, 095102. [CrossRef]
91. Cui, P.; Choi, J.-H.; Chen, W.; Zeng, J.; Shih, C.-K.; Li, Z.; Zhang, Z. Contrasting structural reconstructions, electronic properties, and magnetic orderings along different edges of zigzag transition metal dichalcogenide nanoribbons. *Nano Lett.* **2017**, *17*, 1097–1101. [CrossRef] [PubMed]
92. Seivane, L.F.; Barron, H. Atomic and electronic properties of quasi-one-dimensional MoS_2 nanowires. *J. Mater. Res.* **2013**, *28*, 240–249. [CrossRef] [PubMed]
93. Li, W.; Zhang, G.; Guo, M.; Zhang, Y.-W. Strain-tunable electronic and transport properties of MoS_2 nanotubes. *Nano Res.* **2014**, *7*, 518–527. [CrossRef]
94. Jin, H.; Baek, B.; Kim, D.; Wu, F.; Batteas, J.D.; Cheon, J.; Son, D.H. Effects of direct solvent-quantum dot interaction on the optical properties of colloidal monolayer WS_2 quantum dots. *Nano Lett.* **2017**, *17*, 7471–7477. [CrossRef] [PubMed]
95. Splendiani, A.; Sun, L.; Zhang, Y.; Li, T.; Kim, J.; Chim, C.-Y.; Galli, G.; Wang, F. Emerging Photoluminescence in Monolayer MoS_2. *Nano Lett.* **2010**, *10*, 1271–1275. [CrossRef] [PubMed]
96. Lee, C.; Yan, H.; Brus, L.E.; Heinz, T.F.; Hone, J.; Ryu, S. Anomalous lattice vibrations of single and few-layer MoS_2. *ACS Nano* **2010**, *4*, 2695–2700. [CrossRef] [PubMed]
97. Huang, J.-K.; Pu, J.; Hsu, C.-L.; Chiu, M.-H.; Juang, Z.-Y.; Chang, Y.-H.; Chang, W.-H.; Iwasa, Y.; Takenobu, T.; Li, L.-J. Large-area synthesis of highly crystalline WSe_2 monolayers and device applications. *ACS Nano* **2014**, *8*, 923–930. [CrossRef] [PubMed]
98. Kalantar-zadeh, K.; Ou, J.Z.; Daeneke, Z.; Strano, M.S.; Pumera, M.; Gras, S.L. Two-dimensional transition metal dichalcogenides in biosystems. *Adv. Funct. Mater.* **2015**, *25*, 5086–5099. [CrossRef]
99. Zhang, Y.; Zheng, B.; Zhu, C.; Zhang, X.; Tan, C.; Li, H.; Chen, B.; Yang, J.; Chen, J.; Huang, Y.; et al. Single-layer transition metal dichalcogenide nanosheet-based nanosensors for rapid, sensitive, and multiplexed detection of DNA. *Adv. Mater.* **2015**, *27*, 935–939. [CrossRef] [PubMed]
100. Gutiérrez, H.R.; Perea-López, N.; Elías, A.L.; Berkdemir, A.; Wang, B.; Lv, R.; López-Urías, F.; Crespi, V.H.; Terrones, H.; Terrones, M. Extraordinary room-temperature photoluminescence in triangular WS_2 monolayers. *Nano Lett.* **2013**, *13*, 3447–3454. [CrossRef] [PubMed]
101. Molina-Sánchez, A.; Wirtz, L. Phonons in single-layer and few-layer MoS_2 and WS_2. *Phys. Rev. B* **2011**, *84*, 155413. [CrossRef]
102. Kuroda, N.; Nishina, Y. Davydov splitting of degenerate lattice modes in the layer compound GaS. *Phys. Rev. B* **1979**, *19*, 1312–1315. [CrossRef]
103. Li, H.; Lu, G.; Wang, Y.; Yin, Z.; Cong, C.; He, Q.; Wang, L.; Ding, F.; Yu, T.; Zhang, H. Mechanical exfoliation and characterization of single- and few-layer nanosheets of WSe_2, TaS_2, and $TaSe_2$. *Small* **2013**, *9*, 1974–1981. [CrossRef] [PubMed]
104. Tonndorf, P.; Schmidt, R.; Böttger, P.; Zhang, X.; Börner, J.; Liebig, A.; Albrecht, M.; Kloc, C.; Gordan, O.; Zahn, D.R.T.; et al. Photoluminescence emission and Raman response of monolayer MoS_2, $MoSe_2$, and WSe_2. *Opt. Express* **2013**, *21*, 4908–4916. [CrossRef] [PubMed]
105. Ioannou, D.; Griffin, D.K. Nanotechnology and molecular cytogenetics: The future has not yet arrived. *Nano Rev.* **2010**, *1*, 5117. [CrossRef] [PubMed]
106. Chen, Y.; Xi, J.; Dumcenco, D.O.; Liu, Z.; Suenaga, K.; Wang, D.; Shuai, Z.; Huang, Y.-S.; Xie, L. Tunable band gap photoluminescence from atomically thin transition-metal dichalcogenide alloys. *ACS Nano* **2013**, *7*, 4610–4616. [CrossRef] [PubMed]
107. Yang, L.; Fu, Q.; Wang, W.; Huang, J.; Huang, J.; Zhang, J.; Xiang, B. Large-area synthesis of monolayered $MoS_{2(1-x)}Se_{2x}$ with a tunable band gap and its enhanced electrochemical catalytic activity. *Nanoscale* **2015**, *7*, 10490–10497. [CrossRef] [PubMed]
108. Fu, Q.; Yang, L.; Wang, W.; Han, A.; Huang, J.; Du, P.; Fan, Z.; Zhang, J.; Xiang, B. Synthesis and enhanced electrochemical catalytic performance of monolayer $WS_{2(1-x)}Se_{2x}$ with a tunable band gap. *Adv. Mater.* **2015**, *27*, 4732–4738. [CrossRef] [PubMed]

109. Huang, J.; Wang, W.; Fu, Q.; Yang, L.; Zhang, K.; Zhang, J.; Xiang, B. Stable electrical performance observed in large-scale monolayer $WSe_{2(1-x)}S_{2x}$ with tunable band gap. *Nanotechnology* **2016**, *27*, 13. [CrossRef] [PubMed]
110. Castellanos-Gomez, A.; Roldán, R.; Cappelluti, E.; Buscema, M.; Guinea, F.; van der Zant, H.S.J.; Steele, G.A. Local strain engineering in atomically thin MoS_2. *Nano Lett.* **2013**, *13*, 5361–5366. [CrossRef] [PubMed]
111. Conley, H.J.; Wang, B.; Ziegler, J.I.; Haglund, R.F., Jr.; Pantelides, S.T.; Bolotin, K.I. Bandgap engineering of strained monolayer and bilayer MoS_2. *Nano Lett.* **2013**, *13*, 3626–3630. [CrossRef] [PubMed]
112. Pan, H.; Zhang, Y.-W. Tuning the electronic and magnetic properties of MoS_2 nanoribbons by strain engineering. *J. Phys. Chem. C* **2012**, *116*, 11752–11757. [CrossRef]
113. Mao, N.; Chen, Y.; Liu, D.; Zhang, J.; Xie, L. Solvatochromic effect on the photoluminescence of MoS_2 monolayers. *Small* **2013**, *9*, 1312–1315. [CrossRef] [PubMed]
114. Ahn, G.H.; Amani, M.; Rasool, H.; Lien, D.-H.; Mastandrea, J.P.; Ager, J.W., III; Dubey, M.; Chrzan, D.C.; Minor, A.M.; Javey, A. Strain-engineered growth of two-dimensional materials. *Nat. Commum.* **2017**, *8*, 608. [CrossRef] [PubMed]
115. Chen, S.-F.; Wu, Y.-R. Electronic properties of MoS_2 nanoribbon with strain using tight-binding method. *Phys. Status Solidi B* **2017**, *254*, 1600565. [CrossRef]
116. Yue, Q.; Chang, S.; Kang, J.; Zhang, X.; Shao, Z.; Qin, S.; Li, J. Bandgap tuning in armchair MoS_2 nanoribbon. *J. Phys. Condens. Matter* **2012**, *24*, 335501. [CrossRef] [PubMed]
117. Bertolazzi, S.; Brivio, J.; Kis, A. Stretching and breaking of ultrathin MoS_2. *ACS Nano* **2011**, *5*, 9703–9709. [CrossRef] [PubMed]
118. Cai, L.; He, J.; Liu, Q.; Yao, T.; Chen, L.; Yan, W.; Hu, F.; Jiang, Y.; Zhao, Y.; Hu, T.; et al. Vacancy-induced ferromagnetism of MoS_2 nanosheets. *J. Am. Chem. Soc.* **2015**, *137*, 2622–2627. [CrossRef] [PubMed]
119. Jo, S.; Costanzo, D.; Berger, H.; Morpurgo, A.F. Electrostatically induced superconductivity at the Surface of WS_2. *Nano Lett.* **2015**, *15*, 1197–1202. [CrossRef] [PubMed]
120. Kaplan-Ashiri, I.; Cohen, S.R.; Gartsman, K.; Rosentsveig, R.; Seifert, G.; Tennea, R. Mechanical behavior of individual WS_2 nanotubes. *J. Mater. Res.* **2004**, *19*, 454–459. [CrossRef]
121. Ataca, C.; Sahin, H.; Aktürk, E.; Ciraci, S. Mechanical and electronic properties of MoS_2 nanoribbons and their defects. *J. Phys. Chem. C* **2011**, *115*, 3934–3941. [CrossRef]
122. Zhu, Z.Y.; Cheng, Y.C.; Schwingenschlögl, U. Giant spin-orbit-induced spin splitting in two-dimensional transition-metal dichalcogenide semiconductors. *Phys. Rev. B* **2011**, *84*, 153402. [CrossRef]
123. Zhang, J.; Soon, J.M.; Loh, K.P.; Yin, J.; Ding, J.; Sullivian, M.B.; Wu, P. Magnetic molybdenum disulfide nanosheet films. *Nano Lett.* **2007**, *7*, 2370–2376. [CrossRef] [PubMed]
124. Zheng, H.; Yang, B.; Wang, D.; Han, R.; Du, X.; Yan, Y. Tuning magnetism of monolayer MoS_2 by doping vacancy and applying strain. *Appl. Phys. Lett.* **2014**, *104*, 132403. [CrossRef]
125. Somoano, R.B.; Hadek, V.; Rembaum, A. The alkaline earth intercalates of molybdenum disulfide. *J. Chem. Phys.* **1975**, *62*, 1068–1073. [CrossRef]
126. Woollam, J.A. Physics and chemistry of MoS_2 intercalation compounds. *Mater. Sci. Eng.* **1977**, *31*, 289–295. [CrossRef]
127. Woolam, J.A.; Somoano, R.B. Superconducting critical fields of alkali and alkaline-earth intercalates of MoS_2. *Phys. Rev. B* **1976**, *13*, 3843. [CrossRef]
128. Taniguchi, K.; Matsumoto, A.; Shimotani, H.; Takagi, H. Electric-field-induced superconductivity at 9.4 K in a layered transition metal disulphide MoS_2. *Appl. Phys. Lett.* **2012**, *101*, 042603. [CrossRef]
129. Shi, W.; Ye, J.; Zhang, Y.; Suzuki, R.; Yoshida, M.; Miyazaki, J.; Saito, N.I.Y.; Iwasa, Y. Superconductivity series in transition metal dichalcogenides by ionic gating. *Sci. Rep.* **2015**, *5*, 12534. [CrossRef] [PubMed]
130. Wang, F.; Stepanov, P.; Gray, M.; Lau, C.N.; Itkis, M.E.; Haddon, R.C. Ionic liquid gating of suspended MoS_2 field effect transistor devices. *Nano Lett.* **2015**, *15*, 5284–5288. [CrossRef] [PubMed]
131. Wu, C.-L.; Yuan, H.; Li, Y.; Gong, Y.; Hwang, H.Y.; Cui, Y. Gate-induced metal–insulator transition in MoS_2 by solid superionic conductor LaF_3. *Nano Lett.* **2018**, *18*, 2387–2392. [CrossRef] [PubMed]
132. Costanzo, D.; Jo, S.; Berger, H.; Morpurgo, A.F. Gate-induced superconductivity in atomically thin MoS_2 crystals. *Nat. Nanotechnol.* **2016**, *11*, 339–344. [CrossRef] [PubMed]
133. Fang, Y.; Pan, J.; He, J.; Luo, R.; Wang, D.; Che, X.; Bu, K.; Zhao, W.; Liu, P.; Mu, G.; et al. Structure re-determination and superconductivity observation of bulk 1T MoS_2. *Angew. Chem. Int. Ed.* **2018**, *130*, 1246–1249. [CrossRef]

134. Yao, Y.; Lin, Z.; Li, Z.; Song, X.; Moona, K.-S.; Wong, C.-P. Large-scale production of two-dimensional nanosheets. *J. Mater. Chem.* **2012**, *22*, 13494–13499. [CrossRef]
135. Peng, J.; Wu, J.; Li, X.; Zhou, Y.; Yu, Z.; Guo, Y.; Wu, J.; Lin, Y.; Li, Z.; Wu, X.; et al. Very large-sized transition metal dichalcogenides monolayers from fast exfoliation by manual shaking. *J. Am. Chem. Soc.* **2017**, *139*, 9019–9025. [CrossRef] [PubMed]
136. Gerchman, D.; Alves, A.K. Solution-processable exfoliation and suspension of atomically thin WSe_2. *J. Colloid Interface Sci.* **2016**, *468*, 247–252. [CrossRef] [PubMed]
137. Gopalakrishnan, D.; Damien, D.; Shaijumon, M.M. MoS_2 quantum dot-interspersed exfoliated MoS_2 nanosheets. *ACS Nano* **2014**, *8*, 5297–5303. [CrossRef] [PubMed]
138. Zhao, X.; He, D.; Wang, Y.; Fu, C. Facile fabrication of tungsten disulfide quantum dots (WS_2 QDs) as effective probes for fluorescence detection of dopamine (DA). *Mater. Chem. Phys.* **2018**, *207*, 130–134. [CrossRef]
139. Bai, X.; Wang, J.; Mu, X.; Yang, J.; Liu, H.; Xu, F.; Jing, Y.; Liu, L.; Xue, X.; Dai, H.; et al. Ultrasmall WS_2 quantum dots with visible fluorescence for protection of cells and animal models from radiation-induced damages. *ACS Biomater. Sci. Eng.* **2017**, *3*, 460–470. [CrossRef]
140. Khan, U.; Porwal, H.; O'Neill, A.; Nawaz, K.; May, P.; Coleman, J.N. Solvent-exfoliated graphene at extremely high concentration. *Langmuir* **2011**, *27*, 9077–9082. [CrossRef] [PubMed]
141. Lu, X.; Utama, M.I.B.; Zhang, J.; Zhao, Y.; Xiong, Q. Layer-by-layer thinning of MoS_2 by thermal annealing. *Nanoscale* **2013**, *5*, 8904–8908. [CrossRef] [PubMed]
142. Wu, J.; Li, H.; Yin, Z.; Li, H.; Liu, J.; Cao, X.; Zhang, Q.; Zhang, H. Layer thinning and etching of mechanically exfoliated MoS_2 nanosheets by thermal annealing in air. *Small* **2013**, *9*, 3314–3319. [PubMed]
143. Liu, P.; Li, H.; Yang, L.; Zhao, B.; Li, M.; Xiang, B. Rational synthesis of bandgap-tunable $MS_{2(1-x)}Se_{2x}$ (M = Mo, W) alloys and their physical properties. *J. Alloys Compd.* **2017**, *710*, 628–634. [CrossRef]
144. Wang, S.; Li, K.; Chen, Y.; Chen, H.; Ma, M.; Feng, J.; Zhao, Q.; Shi, S. Biocompatible PEGylated MoS_2 nanosheets: Controllable bottom-up synthesis and highly efficient photothermal regression of tumor. *Biomaterials* **2015**, *39*, 206–217. [CrossRef] [PubMed]
145. Mohanty, B.; Ghorbani-Asl, M.; Kretschmer, S.; Ghosh, A.; Guha, P.; Panda, S.K.; Jena, B.; Krasheninnikov, A.V.; Jena, B.K. MoS_2 quantum dots as efficient catalyst materials for the oxygen evolution reaction. *ACS Catal.* **2018**, *8*, 1683–1689. [CrossRef]
146. Vadivelmurugana, A.; Anbazhagana, R.; Tsai, H.-C. Preparation of fluorescent MoS_2 quantum dots conjugated with various ligands, and its fluorescence imaging. *Mater. Lett.* **2018**, *218*, 285–289. [CrossRef]
147. Wang, Y.; Ni, Y. Molybdenum disulfide quantum dots as a photoluminescence sensing platform for 2,4,6-trinitrophenol detection. *Anal. Chem.* **2014**, *86*, 7463–7470. [CrossRef] [PubMed]
148. Shi, J.; Ma, D.; Han, G.-F.; Zhang, Y.; Ji, Q.; Gao, T.; Sun, J.; Song, X.; Li, C.; Zhang, Y.; et al. Controllable growth and transfer of monolayer MoS_2 on Au foils and its potential application in hydrogen evolution reaction. *ACS Nano* **2014**, *8*, 10196–10204. [CrossRef] [PubMed]
149. Lee, J.; Pak, S.; Giraud, P.; Lee, Y.-W.; Cho, Y.; Hong, J.; Jang, A.-R.; Chung, H.-S.; Hong, W.-K.; Jeong, H.Y.; et al. Thermodynamically stable synthesis of large-scale and highly crystalline transition metal dichalcogenide monolayers and their unipolar n-n heterojunction devices. *Adv. Mater.* **2017**, *29*, 1702206. [CrossRef] [PubMed]
150. Chen, J.; Zhao, X.; Tan, S.J.R.; Xu, H.; Wu, B.; Liu, B.; Fu, D.; Fu, W.; Geng, D.; Liu, Y.; et al. Chemical vapor deposition of large-size monolayer $MoSe_2$ crystals on molten glass. *J. Am. Chem. Soc.* **2017**, *139*, 1073–1076. [CrossRef] [PubMed]
151. Vilá, R.A.; Momeni, K.; Wang, Q.; Bersch, B.M.; Lu, N.; Kim, M.J.; Chen, L.Q.; Robinso, J.A. Bottom-up synthesis of vertically oriented two-dimensional materials. *2D Mater.* **2016**, *3*, 041003. [CrossRef]
152. Zhang, F.; Momeni, K.; AlSaud, M.A.; Azizi, A.; Hainey, M., Jr.; Redwing, J.M.; Chen, L.-Q.; Alem, N. Controlled synthesis of 2D transition metal dichalcogenides: From vertical to planar MoS_2. *2D Mater.* **2017**, *4*, 025029. [CrossRef]
153. Fu, Q.; Wang, W.; Yang, L.; Huang, J.; Zhang, J.; Xiang, B. Controllable synthesis of high quality monolayer WS_2 on a SiO_2/Si substrate by chemical vapor deposition. *RSC Adv.* **2015**, *5*, 15795–15799. [CrossRef]
154. Zhou, J.; Lin, J.; Huang, X.; Zhou, Y.; Chen, Y.; Xia, J.; Wang, H.; Xie, Y.; Yu, H.; Lei, J.; et al. A library of atomically thin metal chalcogenides. *Nature* **2018**, *556*, 355–359. [CrossRef] [PubMed]

155. Yang, P.; Zou, X.; Zhang, Z.; Hong, M.; Shi, J.; Chen, S.; Shu, J.; Zhao, L.; Jiang, S.; Zhou, X.; et al. Batch production of 6-inch uniform monolayer molybdenum disulfide catalyzed by sodium in glass. *Nat. Commun.* **2018**, *9*, 979. [CrossRef] [PubMed]
156. Yang, L.; Wang, W.; Fu, Q.; Zhang, J.; Xiang, B. $MoS_{2(1-x)}Se_{2x}$ nanobelts for enhanced hydrogen evolution. *Electrochim. Acta* **2015**, *185*, 236–241. [CrossRef]
157. Lim, Y.R.; Han, J.K.; Kim, S.K.; Lee, Y.B.; Yoon, Y.; Kim, S.J.; Min, B.K.; Kim, Y.; Jeon, C.; Won, S.; et al. Roll-to-roll production of layer-controlled molybdenum disulfide: A platform for 2D semiconductor-based industrial applications. *Adv. Mater.* **2017**, *30*, 1705270. [CrossRef] [PubMed]
158. Chen, J.; Kuriyama, N.; Yuan, H.; Takeshita, H.T.; Sakai, T. Electrochemical hydrogen storage in MoS_2 nanotubes. *J. Am. Chem. Soc.* **2001**, *123*, 11813–11814. [CrossRef] [PubMed]
159. Kis, A.; Mihailovic, D.; Remskar, M.; Mrzel, A.; Jesih, A.; Piwonski, I.; Kulik, A.J.; Benoît, W.; Forró, L. Shear and Young's Moduli of MoS_2 nanotube ropes. *Adv. Mater.* **2003**, *15*, 733–736. [CrossRef]
160. Muratore, C.; Hu, J.J.; Wang, B.; Haque, M.A.; Bultman, J.E.; Jespersen, M.L.; Shamberger, P.J.; McConney, M.E.; Naguy, R.D.; Voevodin, A.A. Continuous ultra-thin MoS_2 films grown by low-temperature physical vapor deposition. *Appl. Phys. Lett.* **2014**, *104*, 261604. [CrossRef]
161. Wu, S.; Huang, C.; Aivazian, G.; Ross, J.S.; Cobden, D.H.; Xu, X. Vapor-solid growth of high optical quality MoS_2 monolayers with near-unity valley polarization. *ACS Nano* **2013**, *7*, 2768–2772. [CrossRef] [PubMed]
162. Zhao, M.; Ye, Y.; Han, Y.; Xia, Y.; Zhu, H.; Wang, S.; Wang, Y.; Muller, D.A.; Zhang, X. Large-scale chemical assembly of atomically thin transistors and circuits. *Nat. Nanotechnol.* **2016**, *11*, 954–959. [CrossRef] [PubMed]
163. English, C.D.; Shine, G.; Dorgan, V.E.; Saraswat, K.C.; Pop, E. Improved contacts to MoS_2 transistors by ultra-high vacuum metal deposition. *Nano Lett.* **2016**, *16*, 3824–3830. [CrossRef] [PubMed]
164. Ilatikhameneh, H.; Ameen, T.; Novakovic, B.; Tan, Y.; Klimeck, G.; Rahman, R. Saving Moore's Law down to 1 nm channels with anisotropic effective mass. *Sci. Rep.* **2016**, *6*, 31501. [CrossRef] [PubMed]
165. Ling, X.; Lin, Y.; Ma, Q.; Wang, Z.; Song, Y.; Yu, L.; Huang, S.; Fang, W.; Zhang, X.; Hsu, A.L.; et al. Parallel stitching of two-dimensional materials. *Adv. Mater.* **2016**, *28*, 2322–2329. [CrossRef] [PubMed]
166. Xu, K.; Chen, D.; Yang, F.; Wang, Z.; Yin, L.; Wang, F.; Cheng, R.; Liu, K.; Xiong, J.; Liu, Q.; et al. Sub-10 nm nanopatterns architecture for 2D materials field-effect transistors. *Nano Lett.* **2017**, *17*, 1065–1070. [CrossRef] [PubMed]
167. Jena, D.; Konar, A. Enhancement of carrier mobility in semiconductor nanostructures by dielectric engineering. *Phys. Rev. Lett.* **2007**, *98*, 136805. [CrossRef] [PubMed]
168. Lopez-Sanchez, O.; Lembke, D.; Kayci, M.; Radenovic, A.; Kis, A. Ultrasensitive photodetectors based on monolayer MoS_2. *Nat. Nanotechnol.* **2013**, *8*, 497–501. [CrossRef] [PubMed]
169. Yin, Z.; Li, H.; Li, H.; Jiang, L.; Shi, Y.; Sun, Y.; Lu, G.; Zhang, Q.; Chen, X.; Zhang, H. Single-layer MoS_2 phototransistors. *ACS Nano* **2012**, *6*, 74–80. [CrossRef] [PubMed]
170. Cheng, R.; Li, D.; Zhou, H.; Wang, C.; Yin, A.; Jiang, S.; Liu, Y.; Chen, Y.; Huang, Y.; Duan, X. Electroluminescence and photocurrent generation from atomically sharp WSe_2/MoS_2 heterojunction p-n diodes. *Nano Lett.* **2014**, *14*, 5590–5597. [CrossRef] [PubMed]
171. Xia, F.; Wang, H.; Xiao, D.; Dubey, M.; Ramasubramaniam, A. Two-dimensional material nanophotonics. *Nat. Photonics* **2014**, *8*, 899–907. [CrossRef]
172. Yoon, Y.; Ganapathi, K.; Salahuddin, S. How good can monolayer MoS_2 transistors be? *Nano Lett.* **2011**, *11*, 3768–3773. [CrossRef] [PubMed]
173. Late, D.J.; Liu, B.; Matte, R.H.S.S.; Dravid, V.P.; Rao, C.N.R. Hysteresis in single-layer MoS_2 field effect transistors. *ACS Nano* **2012**, *6*, 5635–5641. [CrossRef] [PubMed]
174. Lee, C.-H.; Lee, G.-H.; van der Zande, A.M.; Chen, W.; Li, Y.; Han, M.; Cui, X.; Arefe, G.; Nuckolls, C.; Heinz, T.F.; et al. Atomically thin p-n junctions with van der Waals heterointerfaces. *Nat. Nanotechnol.* **2014**, *9*, 676–681. [CrossRef] [PubMed]
175. Masuko, K.; Shigematsu, M.; Hashiguchi, T.; Fujishima, D.; Kai, M.; Yoshimura, N.; Yamaguchi, T.; Ichihashi, Y.; Mishima, T.; Matsubara, N.; et al. Achievement of more than 25% conversion efficiency with crystalline silicon heterojunction solar cell. *IEEE J. Photovolt.* **2014**, *4*, 1433–1435. [CrossRef]
176. Green, M.A.; Emery, K.; Hishikawa, Y.; Warta, W.; Dunlop, E.D. Solar cell efficiency tables (version 48). *Prog. Photovolt. Res. Appl.* **2016**, *24*, 905–913. [CrossRef]

177. Danos, L.; Parel, T.; Markvart, T.; Barrioz, V.; Brooks, W.S.M.; Irvine, S.J.C. Increased efficiencies on CdTe solar cells via luminescence down-shifting with excitation energy transfer between dyes. *Sol. Energy Mater. Sol. Cells* **2012**, *98*, 486–490. [CrossRef]
178. Acciarria, M.; Donnea, A.L.; Marchionnab, M.; Meschiab, M.; Parravicinia, J.; Gasparottoc, A.; Binettia, S. CIGS thin films grown by hybrid sputtering-evaporation method: Properties and PV performance. *Sol. Energy* **2018**. [CrossRef]
179. Tributsch, H.; Bennett, J.C. Electrochemistry and photochemistry of MoS_2 layer crystals. I. *J. Electroanal. Chem. Interfacial Electrochem.* **1977**, *81*, 97–111. [CrossRef]
180. Hinnemann, B.; Moses, P.G.; Bonde, J.; Jørgensen, K.P.; Nielsen, J.H.; Horch, S.; Chorkendorff, I.; Nørskov, J.K. Biomimetic hydrogen evolution: MoS_2 nanoparticles as catalyst for hydrogen evolution. *J. Am. Chem. Soc.* **2005**, *127*, 5308–5309. [CrossRef] [PubMed]
181. Jaramillo, T.F.; Jørgensen, K.P.; Bonde, J.; Nielsen, J.H.; Horch, S.; Chorkendorff, I. Identification of active edge sites for electrochemical H_2 evolution from MoS_2 nanocatalysts. *Science* **2007**, *317*, 100–102. [CrossRef] [PubMed]
182. Liao, L.; Zhu, J.; Bian, X.; Zhu, L.; Scanlon, M.D.; Girault, H.H.; Liu, B. MoS_2 formed on mesoporous graphene as a highly active catalyst for hydrogen evolution. *Adv. Funct. Mater.* **2013**, *23*, 5326–5333. [CrossRef]
183. Voiry, D.; Salehi, M.; Silva, R.; Fujita, T.; Chen, M.; Asefa, T.; Shenoy, V.B.; Eda, G.; Chhowalla, M. Conducting MoS_2 nanosheets as catalysts for hydrogen evolution reaction. *Nano Lett.* **2013**, *13*, 6222–6227. [CrossRef] [PubMed]
184. Wang, H.; Kong, D.; Johanes, P.; Cha, J.J.; Zheng, G.; Yan, K.; Liu, N.; Cui, Y. $MoSe_2$ and WSe_2 nanofilms with vertically aligned molecular layers on curved and rough surfaces. *Nano Lett.* **2013**, *13*, 3426–3433. [CrossRef] [PubMed]
185. Wu, Z.; Fang, B.; Wang, Z.; Wang, C.; Liu, Z.; Liu, F.; Wang, W.; Alfantazi, A.; Wang, D.; Wilkinson, D.P. MoS_2 Nanosheets: A designed structure with high active site density for the hydrogen evolution reaction. *ACS Catal.* **2013**, *3*, 2101–2107. [CrossRef]
186. Deng, J.; Li, H.; Xiao, J.; Tu, Y.; Deng, D.; Yang, H.; Tian, H.; Li, J.; Rena, P.; Bao, X. Triggering the electrocatalytic hydrogen evolution activity of the inert two dimensional MoS_2 surface via single-atom metal doping. *Energy Environ. Sci.* **2015**, *8*, 1594–1601. [CrossRef]
187. Appel, A.M.; DuBois, D.L.; DuBois, M.R. Molybdenum-sulfur dimers as electrocatalysts for the production of hydrogen at low overpotentials. *J. Am. Chem. Soc.* **2005**, *127*, 12717–12726. [CrossRef] [PubMed]
188. Ou, G.; Fan, P.; Ke, X.; Xu, Y.; Huang, K.; Wei, H.; Yu, W.; Zhang, H.; Zhong, M.; Wu, H.; et al. Defective molybdenum sulfide quantum dots as highly active hydrogen evolution electrocatalysts. *Nano Res.* **2018**, *11*, 751–761. [CrossRef]
189. Zhu, C.; Zeng, Z.; Li, H.; Li, F.; Fan, C.; Zhang, H. Single-layer MoS_2-based nanoprobes for homogeneous detection of biomolecules. *J. Am. Chem. Soc.* **2013**, *135*, 5998–6001. [CrossRef] [PubMed]
190. Wang, S.; Chen, Y.; Li, X.; Gao, W.; Zhang, L.; Liu, J.; Zheng, Y.; Chen, H.; Shi, J. Injectable 2D MoS_2-integrated drug delivering implant for highly efficient NIR-triggered synergistic tumor hyperthermia. *Adv. Mater.* **2015**, *27*, 7117–7122. [CrossRef] [PubMed]
191. Xu, S.; Li, D.; Wu, P. One-pot, facile, and versatile synthesis of monolayer MoS_2/WS_2 quantum dots as bioimaging probes and efficient electrocatalysts for hydrogen evolution reaction. *Adv. Funct. Mater.* **2015**, *25*, 1127–1136. [CrossRef]
192. Vesborg, P.C.K.; Seger, B.; Chorkendorff, I. Recent development in hydrogen evolution reaction catalysts and their practical implementation. *J. Phys. Chem. Lett.* **2015**, *6*, 951–957. [CrossRef] [PubMed]
193. Shia, Y.; Zhang, B. Recent advances in transition metal phosphide nanomaterials: Synthesis and applications in hydrogen evolution reaction. *Chem. Soc. Rev.* **2016**, *45*, 1529–1541. [CrossRef] [PubMed]
194. Lukowski, M.A.; Daniel, A.S.; Meng, F.; Forticaux, A.; Li, L.; Jin, S. Enhanced hydrogen evolution catalysis from chemically exfoliated metallic MoS_2 nanosheets. *J. Am. Chem. Soc.* **2013**, *135*, 10274–10277. [CrossRef] [PubMed]
195. Li, Y.; Wang, H.; Xie, L.; Liang, Y.; Hong, G.; Dai, H. MoS_2 nanoparticles grown on graphene: An advanced catalyst for the hydrogen evolution reaction. *J. Am. Chem. Soc.* **2011**, *133*, 7296–7299. [CrossRef] [PubMed]
196. Yan, Y.; Ge, X.; Liu, Z.; Wang, J.-Y.; Leea, J.-M.; Wang, X. Facile synthesis of low crystalline MoS_2 nanosheet-coated CNTs for enhanced hydrogen evolution reaction. *Nanoscale* **2013**, *5*, 7768–7771. [CrossRef] [PubMed]

197. Chen, Z.; Cummins, D.; Reinecke, B.N.; Clark, E.; Sunkara, M.K.; Jaramillo, T.F. Core-shell MoO_3-MoS_2 nanowires for hydrogen evolution: A functional design for electrocatalytic materials. *Nano Lett.* **2011**, *11*, 4168–4175. [CrossRef] [PubMed]
198. Huang, Y.; Miao, Y.-E.; Zhang, L.; Tjiu, W.W.; Panb, J.; Liu, T. Synthesis of few-layered MoS_2 nanosheet-coated electrospun SnO_2 nanotube heterostructures for enhanced hydrogen evolution reaction. *Nanoscale* **2014**, *6*, 10673–10679. [CrossRef] [PubMed]